Simulation of a tunable coupler for implementing two-qubit gates between transmon qubits

Severi Rissanen

School of Science

Bachelor's thesis
Espoo 20.9.2018

Supervisor

Prof. Matti Kaivola

Advisors

Dr. Mikko Möttönen

M.Sc. Joni Ikonen

**Aalto University
School of Science**

Aalto University
School of Science

Aalto University, P.O. BOX 11000, 00076 AALTO
www.aalto.fi
Abstract of the bachelor's thesis

Author Severi Rissanen	
Title Simulation of a tunable coupler for implementing two-qubit gates between transmon qubits	
Degree programme Engineering Physics and Mathematics	
Major Engineering Physics	**Code of major** SCI3028
Supervisor Prof. Matti Kaivola	
Advisors Dr. Mikko Möttönen, M.Sc. Joni Ikonen	
Date 20.9.2018 **Number of pages** 26+6	**Language** English

Abstract

Quantum computers are, as of yet not realized on the large scale, devices that can solve some problems exponentially faster than any current classical computer. Their operation principle is to encode a computational process in the temporal evolution of multiple coupled two-state quantum mechanical systems, qubits. Important elementary building blocks of such devices are two-qubit logic gates which arise from interactions between two qubits. On a quantum computer, the algorithms are implemented by combining multiple one- and two-qubit gates to reach the desired time evolution.

In this thesis, a tunable coupler scheme proposed by Yan. et al (2018) for the implementation of two-qubit gates is studied by simulating an example system. The simulated system consists of three superconducting transmon qubits capacitively coupled to each other. One of the qubits operates as a tunable coupler between the other two, and by adjusting its frequency, the iSWAP gate is realized. It is found that gate errors of below 10^{-5} can be reached with gate durations of 100 ns for a non-dissipative system by controlling the coupler frequency with a sine-shaped pulse. Two other control pulses are compared, and it is observed that the pulse shape has a large effect when attempting to reach very low errors.

Keywords quantum computing, two-qubit gate, iSWAP, transmon, tunable coupler

Preface

This thesis summarizes the work I carried out over the course of three months as a summer student in 2018 in the Quantum Computing and Devices group at Aalto university. I would like to thank Joni Ikonen for guidance and help throughout the project and Mikko Möttönen for valuable insights and the opportunity to work with this subject. I also thank Matti Kaivola for agreeing to act as the supervisor of this thesis.

Otaniemi, 20.9.2018

Severi Rissanen

Contents

1 Introduction

Quantum computers are future devices that are, in theory, able to solve problems that are not tractable for classical computers [1]. They work by exploiting the laws of quantum mechanics to execute algorithms allowing a large speedup compared with known classical algorithms in some cases. Notable algorithms that are able to use quantum computers for such advantage are Shor's algorithm for factoring large numbers [2] and Grover's algorithm for database searches [3]. Another important area where quantum devices might have a significant advantage compared with classical computers is the simulation of quantum systems [4], first proposed by Richard Feynman in 1982 [5].

Many different prototypes of quantum computers have been envisioned and developed. Superconducting circuits provide one of the most promising schemes to implement the elementary building blocks of quantum computers, quantum bits, or qubits. The use of superconducting circuits in quantum information processing was first proposed over 20 years ago [6], with the idea of using a so-called Cooper pair box, composed of low-capacitance Josephson junctions, as a qubit. A few years later the first experimental realizations of such circuits were achieved [7, 8]. Superconducting qubits have since undergone a rapid development, with the introduction of numerous designs, such as the phase qubit [9], the transmon [10], and the fluxonium qubit [11]. The field remains very active and superconducting quantum computers are advancing towards useful and scalable quantum information processing applications [12].

In this thesis, we simulate a tunable-coupling system proposed by Yan et al. [13] for implementing two-qubit quantum logic gates between transmon qubits. The system functions by using three qubits, one used as a coupler between the other two, to implement gate operations by modulating the resonance frequency of the coupler. This design should be able to reduce certain errors caused by unintentional coupling between qubits. The gate implemented by the system is the iSWAP gate, which has been shown to form a universal set of gates together with single-qubit gates [14], implying that any many-qubit gate can be realized by applying these gates on a many-qubit system. We compare three control pulses with different pulse lengths and amplitudes and find that the shape of the pulse has a strong effect on the resulting gate error.

Section 2 discusses the theoretical background relevant to this thesis. In Sec. 3, we introduce the simulated system and discuss some important matters related to the simulation. Section 4 presents the results of the simulations and finally in Sec. 5 conclusions are drawn and possible improvements to the system are discussed.

2 Theoretical background

In this section, some relevant theoretical concepts are considered. We begin with a short overview of the required theory of quantum mechanics, proceed with the basics of quantum computing, and finish with a discussion on superconducting qubits.

2.1 Relevant concepts in quantum mechanics

2.1.1 Quantization of a physical system

We employ a description of a quantum-mechanical system which proceeds as follows. One begins with the analogue classical system, for which the Lagrangian function is given by

$$L(q_1, \dot{q}_1, q_2, \dot{q}_2, ...) = T(\dot{q}_1, \dot{q}_2, ...) - V(q_1, q_2, ...), \tag{1}$$

where q_i are so-called generalized position coordinates, V is the potential energy and T is the kinetic energy of the system. For the quantization of the system, we need to find the Hamiltonian of the system. For this purpose, the generalized momenta are defined with the identity

$$p_i = \frac{\partial \mathcal{L}}{\partial \dot{q}_i}. \tag{2}$$

The variables q_i and p_i are also called canonical conjugate variables. Using a Legendre transformation one arrives at the Hamiltonian

$$H(q_1, p_1, q_2, p_2, ...) = \sum_i p_i q_i - \mathcal{L}. \tag{3}$$

Classically, the equations of motion could then be derived from the Hamiltonian. In quantum mechanics, however, the system cannot be simply described with a group of position and momentum coordinates. Instead, the state of the system is described with a state vector $|\psi\rangle$ in an abstract vector space, the Hilbert space [15]. The Hamiltonian is then substituted by an operator acting on the state vectors, the Hamiltonian operator $\hat{H}$. It is constructed such that the canonical conjugate variables q_i and p_i in $\mathcal{H}$ are replaced with the corresponding position and momentum operators $\hat{q}_i$ and $\hat{p}_i$. The eigenstates of these operators in the Hilbert space have eigenvalues corresponding to classical position and momentum coordinates. In addition, for all of the pairs $(\hat{q}_i, \hat{p}_i)$ the canonical commutation relation $[\hat{q}_i, \hat{p}_i] = \hat{q}_i\hat{p}_i - \hat{p}_i\hat{q}_i = i\hbar$ is satisfied, where $\hbar$ is the reduced Planck constant [15]. Importantly, the temporal evolution of all state vectors is determined by the Schrödinger equation

$$i\hbar\frac{\partial}{\partial t}|\psi(t)\rangle = \hat{H}|\psi(t)\rangle. \tag{4}$$

2.1.2 Methods for solving the Schrödinger equation

The central question in quantum mechanics is how to solve the Schrödinger equation for different systems. One approach is to use the eigenstates of the time-independent Hamiltonian operator, their time evolution being $|\phi(t)\rangle = e^{-\frac{i}{\hbar}Et}|\phi\rangle$, where E is the

eigenvalue, or in this case the eigenenergy of $|\phi\rangle$. The eigenstates of $\hat{H}$ form an orthogonal basis in the Hilbert space, implying that the evolution of any state $|\psi\rangle$ can be obtained by expressing the state as a linear combination of the eigenstates of the system [15]. Another approach is to define the time evolution operator $\hat{U}(t)$, i.e., $\hat{U}(t)|\psi\rangle = |\psi(t)\rangle$. For time-independent Hamiltonians, we may express it as

$$\hat{U}(t) = e^{-\frac{i}{\hbar}\hat{H}t} = \sum_{k=0}^{\infty} \frac{(-i)^k \hat{H}^k t^k}{k!\hbar^k}, \tag{5}$$

which can be confirmed by inserting $|\psi(t)\rangle = e^{-\frac{i}{\hbar}\hat{H}t}|\psi(0)\rangle$ in Eq. (4). If the Hamiltonian has an explicit time dependence due to, for instance, a driving field, the above methods do not apply. In this case, the evolution of the system is divided into a sequence of periods, for which the Hamiltonian is essentially constant. Thus we obtain

$$|\psi(t)\rangle = e^{-\frac{i}{\hbar}\hat{H}(t-\Delta t)\Delta t}e^{-\frac{i}{\hbar}\hat{H}(t-2\Delta t)\Delta t} \times \cdots \times e^{-\frac{i}{\hbar}\hat{H}(\Delta t)\Delta t}e^{-\frac{i}{\hbar}\hat{H}(0)\Delta t}|\psi\rangle. \tag{6}$$

By taking the limit $\Delta t \to 0$, this description becomes exact. If it holds that $[\hat{H}(t_1), \hat{H}(t_2)] = 0$ for all t_1 and t_2, $\hat{U}(t)$ is brought to a simple form. In this case, the exponents of the time evolution operators are summed together, resulting in

$$|\psi(t)\rangle = e^{-\frac{i}{\hbar}\sum_{k=0}^{N}\hat{H}(k\Delta t)\Delta t}|\psi\rangle. \tag{7}$$

In the limit $\Delta t \to 0$, the sum then becomes an integral. Thus, the time evolution operator is given by

$$\hat{U}(t) = e^{-\frac{i}{\hbar}\int_0^t \hat{H}(t')\mathrm{d}t'}. \tag{8}$$

In general, if $[\hat{H}(t_1), \hat{H}(t_2)] = 0$ does not hold, we write $\hat{U}(t)$ symbolically as

$$\hat{U}(t) = \hat{T}e^{-\frac{i}{\hbar}\int_0^t \hat{H}(t')\mathrm{d}t'}, \tag{9}$$

where $\hat{T}$ is referred to as the time ordering operator [15].

In the case where $\hat{H}$ varies with time very slowly, the time evolution can be understood with the adiabatic theorem. It states that if one changes the Hamiltonian, and thus the eigenstates, of a system continuously and slowly enough, a state vector starting as an eigenstate approximately follows the eigenstate as it changes. Specifically, given an eigenstate $|\phi(t)\rangle$ of the time-dependent Hamiltonian $\hat{H}(t)$, if a state $|\Psi(t)\rangle$ at $t = 0$ is $|\Psi(0)\rangle = |\phi(0)\rangle$, its time evolution is given by [15]

$$|\Psi(t)\rangle = e^{-\frac{i}{\hbar}\int_0^t E(t')\mathrm{d}t'}e^{-i\gamma(t)}|\phi(t)\rangle, \tag{10}$$

where $\gamma(t)$ is the geometric phase

$$\gamma(t) = i\int_0^t \langle\phi(t')|\frac{\partial}{\partial t'}|\phi(t')\rangle \,\mathrm{d}t'. \tag{11}$$

If at the end of the time evolution the Hamiltonian returns to its original form, γ is also called the Berry phase.

2.1.3 Interaction picture

Everything that has been presented above has been in the so-called Schrödinger picture of quantum mechanics. Here, in the absence of explicit time dependencies on operators, the operators stay constant while the state vectors evolve in time. It is often useful to describe the system in the interaction picture, or equivalently in a rotating frame, where both the operators and state vectors carry some of the time dependence. For the interaction picture, we begin by first separating the Hamiltonian operator in the Schrödinger picture $\hat{H}_\mathrm{S}$ into two parts, $\hat{H}_{\mathrm{S},0}$ and $\hat{H}_{\mathrm{S,I}}$ as

$$\hat{H}_\mathrm{S} = \hat{H}_{\mathrm{S},0} + \hat{H}_{\mathrm{S,I}}. \tag{12}$$

The state $|\psi_\mathrm{I}\rangle$ and operators $\hat{A}_\mathrm{I}$ in the interaction picture are related to those in the Schrödinger picture by the relations

$$|\psi_\mathrm{I}(t)\rangle = e^{\frac{i}{\hbar}\hat{H}_{S,0}t} |\psi(t)\rangle \tag{13}$$

$$\hat{A}_\mathrm{I} = e^{\frac{i}{\hbar}\hat{H}_{S,0}t} \hat{A} e^{-\frac{i}{\hbar}\hat{H}_{S,0}t}. \tag{14}$$

Inserting (13) into the Schrödinger equation (4), we obtain

$$i\hbar \frac{\partial}{\partial t}(e^{-\frac{i}{\hbar}\hat{H}_{S,0}t} |\psi_\mathrm{I}(t)\rangle) = \hat{H}_\mathrm{S} e^{-\frac{i}{\hbar}\hat{H}_{S,0}t} |\psi_\mathrm{I}(t)\rangle \tag{15}$$

$$\hat{H}_{\mathrm{S},0} e^{-\frac{i}{\hbar}\hat{H}_{S,0}t} |\psi_\mathrm{I}(t)\rangle + e^{-\frac{i}{\hbar}\hat{H}_{S,0}t} \frac{\partial}{\partial t} |\psi_\mathrm{I}(t)\rangle = (\hat{H}_{\mathrm{S},0} + \hat{H}_{\mathrm{S,I}}) e^{-\frac{i}{\hbar}\hat{H}_{S,0}t} |\psi_\mathrm{I}(t)\rangle \tag{16}$$

$$\frac{\partial}{\partial t} |\psi_\mathrm{I}(t)\rangle = e^{\frac{i}{\hbar}\hat{H}_{S,0}t} \hat{H}_{\mathrm{S,I}} e^{-\frac{i}{\hbar}\hat{H}_{S,0}t} |\psi_\mathrm{I}(t)\rangle \tag{17}$$

$$\frac{\partial}{\partial t} |\psi_\mathrm{I}(t)\rangle = \hat{H}_\mathrm{I} |\psi_\mathrm{I}(t)\rangle , \tag{18}$$

where the interaction Hamiltonian $\hat{H}_\mathrm{I}$ was defined. Thus, the states in the interaction picture follow the Schrödinger equation with the Hamiltonian operator $\hat{H}_\mathrm{I}$. Depending on the system and the chosen $\hat{H}_{\mathrm{S},0}$, it may be more convenient to solve Eq. (18) than the original Schödinger equation.

2.2 Quantum Computing

A central concept in quantum computing is the qubit, a quantum mechanical system with a two-dimensional Hilbert space $\mathscr{H}$[1]. Two orthogonal states in the space are chosen as the computational basis states, $|0\rangle$ and $|1\rangle$, which are in practice usually also the eigenstates of the Hamiltonian. In general, a state of the system is described as a linear combination of these states. It is conventional to represent the state as a column vector where the coefficients of states $|0\rangle$ and $|1\rangle$ are the coefficients of the vector

$$|\psi\rangle = a |0\rangle + b |1\rangle \cong \begin{bmatrix} a \\ b \end{bmatrix}, \tag{19}$$

where $\triangleq$ denotes a representation in the computational basis. Operators are represented as matrices in this basis as[1]

$$\hat{A} \triangleq \begin{bmatrix} \langle 0| \hat{A} |0\rangle & \langle 0| \hat{A} |1\rangle \\ \langle 1| \hat{A} |0\rangle & \langle 1| \hat{A} |1\rangle \end{bmatrix}. \tag{20}$$

To represent the Hilbert space of two qubits, one then takes the tensor product of the Hilbert spaces of the individual qubits, $\mathscr{H}_1 \otimes \mathscr{H}_2$ [1]. A basis for this space is the set of tensor product combinations of the individual basis vectors, $\{|0\rangle \otimes |0\rangle, |0\rangle \otimes |1\rangle, |1\rangle \otimes |0\rangle$, and $|1\rangle \otimes |1\rangle\}$, which we write in short as $\{|00\rangle, |01\rangle, |10\rangle, |11\rangle\}$. States in the four-dimensional space are represented by column vectors with four components as

$$|\psi\rangle = a |00\rangle + b |01\rangle + c |10\rangle + d |11\rangle \triangleq \begin{bmatrix} a \\ b \\ c \\ d \end{bmatrix}. \tag{21}$$

Here, operators are represented by 4×4 matrices. In general, a Hilbert space of n qubits is the tensor product of all single-qubit Hilbert spaces.

The main idea in quantum computing is to design and implement a time evolution operator acting on many-qubit states so that it encodes some computational process. This evolution is usually constructed by externally imposing one and two qubit interactions [1]. The resulting operations are called single- or two-qubit logic gates. For instance, let the Hamiltonian operator of a single-qubit system in the computational basis be

$$\hat{H} \triangleq \begin{bmatrix} 0 & 0 \\ 0 & E \end{bmatrix}. \tag{22}$$

Consequently, the time evolution operator is given by

$$\hat{U}(t) = e^{-\frac{i}{\hbar}\hat{H}t} \triangleq \begin{bmatrix} 1 & 0 \\ 0 & e^{-\frac{i}{\hbar}Et} \end{bmatrix}, \tag{23}$$

which produces a phase shift gate with phase $\phi = -Et/\hbar$ for a given duration of the interaction t. The iSWAP gate is an important two-qubit gate for this thesis. It is represented by

$$\text{iSWAP} = \begin{bmatrix} 1 & 0 & 0 & 0 \\ 0 & 0 & i & 0 \\ 0 & i & 0 & 0 \\ 0 & 0 & 0 & 1 \end{bmatrix}, \tag{24}$$

which is a sufficient two-qubit gate for universal quantum computing, that is, any possible temporal evolution of a many-qubit system may be decomposed into a number of iSWAP gates and single-qubit gates [14].

In practise, qubits may not be true two-state systems, but instead have eigenstates $|0\rangle, |1\rangle, |2\rangle, \ldots$ with increasing eigenenergies $E_0, E_1, E_2, \ldots$. The anharmonicity is a key property of the system in this situation. It is defined to be the angular frequency corresponding to the difference between the two lowest adjacent energy spacings

$$\alpha = (E_2 - E_1)/\hbar - (E_1 - E_0)/\hbar. \tag{25}$$

A nonzero anharmonicity is typically necessary for the system to work as a qubit, since otherwise an addition of energy that excites the state $|0\rangle$ to $|1\rangle$ could also excite the state $|1\rangle$ to the non-computational state $|2\rangle$ [16]. An anharmonicity large enough guarantees that system is in practice never excited to the high-energy states outside the computational space.

2.3   Superconducting qubits

This section gives a short review to superconducting circuits for the implementation of superconducting qubits, and in particular the transmon qubit. We begin with the introduction of a pivotal component in superconducting circuits, the Josephson junction, and proceed with the quantization of the Cooper pair box circuit. In the end, the transmon qubit is discussed.

2.3.1   Josephson junction

The Josephson junction is a central component in superconducting quantum computing. It consists of two superconductors separated by a non-superconducting part, through which electric current flows by tunneling of Cooper pairs between the two superconductors. The difference in the superconducting phase parameter across the junction φ obeys the equations [16]

$$U(t) = \frac{\hbar}{2e}\dot{\varphi}(t) \tag{26}$$

$$I(t) = I_0 \sin[\varphi(t)]. \tag{27}$$

where $U(t)$ and $I(t)$ are the voltage and current across the junction. Note that φ in Eq. (26) behaves similarly as magnetic flux in a normal inductor coil according to Lenz's law

$$U(t) = \dot{\Phi}(t) = L\dot{I}(t). \tag{28}$$

where the $U(t)$ is defined to be difference in the electric potential in the direction where it opposes the change in current. In this sense, the Josephson junction can simply be considered as a nonlinear inductor, with the nonlinearity arising from Eq. (27). The energy stored in a Josephson junction is calculated from the power flowing through it by

$$E = \int_0^t P(t')\mathrm{d}t' = \int_0^t U(t')I(t')\mathrm{d}t' = \int_0^t \frac{\hbar}{2e}\dot{\varphi}(t')I_0 \sin(\varphi(t'))\mathrm{d}t' \tag{29}$$

$$= \frac{\hbar I_0}{2e} \int_0^{\varphi(t)} \sin \varphi' \mathrm{d}\varphi' = E_\mathrm{J}[1 - \cos \varphi(t)]. \tag{30}$$

where the Josephson energy $E_\mathrm{J} = \frac{\hbar I_0}{2e}$ has been defined.

2.3.2   Cooper pair box

The Cooper pair box circuit, referred to as the charge qubit, can be modelled as a Josephson junction combined to a power source with voltage U_g and a capacitor
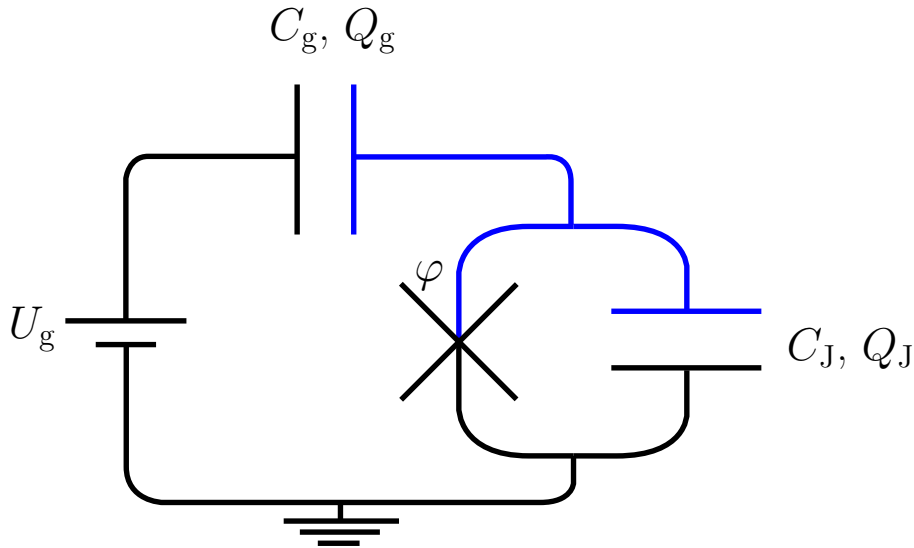
Figure 1: Circuit diagram of a Cooper pair box. The cross-shaped component is the Josephson junction and the section of the circuit colored blue is a superconducting island, to which the Cooper pairs tunnel through the junction.

with capacitance C_g, as shown in Fig. 1. These are also called the gate capacitance and gate voltage. The Josephson junction has also some capacitance of its own, C_J, modelled as an external capacitance in parallel with the junction in the figure. To begin the quantization of the circuit, we first note that there are two types of energy stored in the system, that related to the voltages over the capacitors and the energy related to φ, as in the Josephson junction. We define φ as a generalized position coordinate in Lagrangian mechanics. Thus the energy related to the voltages corresponds to the kinetic energies of the system and energy related to φ corresponds to the potential energy. The Lagrangian of the circuit is given by

$$L = T - V \tag{31}$$

$$T = \frac{1}{2}C_\mathrm{J}U_\mathrm{J}^2 + \frac{1}{2}C_\mathrm{g}(U_\mathrm{J} - U_\mathrm{g})^2 = \frac{1}{2}C_\mathrm{J}\left(\frac{\hbar}{2e}\dot{\varphi}\right)^2 + \frac{1}{2}C_\mathrm{g}(\frac{\hbar}{2e}\dot{\varphi}^2 - U_\mathrm{g})^2 \tag{32}$$

$$V = E_\mathrm{J}(1 - \cos\varphi). \tag{33}$$

Next the generalized momentum p is obtained from

$$p = \frac{\partial L}{\partial \dot{\varphi}} = \left(\frac{\hbar}{2e}\right)^2 (C_\mathrm{J} + C_\mathrm{g})\dot{\varphi} - C_\mathrm{g}U_\mathrm{g}\frac{\hbar}{2e}. \tag{34}$$

Applying the Legendre transformation in Eq. (3) provides us the Hamiltonian of the circuit as

$$H = p\varphi - \mathcal{L} = \frac{\left(p + C_\mathrm{g}U_\mathrm{g}\frac{\hbar}{2e}\right)^2}{2(\frac{\hbar}{2e})^2(C_\mathrm{J} + C_\mathrm{g})} + E_\mathrm{J}(1 - \cos\varphi), \tag{35}$$

where a constant factor $-\frac{1}{2}C_\mathrm{g}U_\mathrm{g}^2$ has been dismissed. The quantization of the circuit is finalized by replacing the canonical position and momentum, φ and p, by the

corresponding operators, $\hat{\varphi}$ and $\hat{p}$ and introducing the canonical commutation relation $[\hat{\varphi}, \hat{p}] = i\hbar$. It is also useful to define a quantity $n_{\mathrm{g}} = -\frac{Q_{\mathrm{g}}}{-2e}$, corresponding to the number of Cooper pairs at the input capacitor caused by the input voltage, and the operator $\hat{n} = -\frac{\hat{p}}{\hbar}$. Thus the Hamiltonian operator assumes the form

$$\hat{H} = \frac{\left(\hat{p} + C_{\mathrm{g}} U_{\mathrm{g}} \frac{\hbar}{2e}\right)^2}{2(\frac{\hbar}{2e})^2 (C_{\mathrm{J}} + C_{\mathrm{g}})} + E_{\mathrm{J}}(1 - \cos\hat{\varphi}) \tag{36}$$

$$= \frac{4e^2}{2(C_{\mathrm{J}} + C_{\mathrm{g}})}(\hat{n} - n_{\mathrm{g}})^2 + E_{\mathrm{J}}(1 - \cos\hat{\varphi}) \tag{37}$$

$$= 4E_{\mathrm{C}}(\hat{n} - n_{\mathrm{g}})^2 + E_{\mathrm{J}}(1 - \cos\hat{\varphi}), \tag{38}$$

where on the last line the charging energy $E_{\mathrm{C}} = \frac{e^2}{2(C_{\mathrm{J}} + C_{\mathrm{g}})}$ has been defined. From the canonical commutation relation $[\hat{\varphi}, \hat{p}] = i\hbar$ it follows that $[\hat{n}, \hat{\varphi}] = i$.

The meaning of the operator $\hat{n}$ may be understood by substituting Eq. (26) in the place of $\dot{\varphi}$ in Eq. (34): we obtain $p = -\hbar \left[\frac{C_{\mathrm{J}} U_{\mathrm{J}}}{-2e} + \frac{C_{\mathrm{g}}(U_{\mathrm{J}} - U_{\mathrm{g}})}{-2e}\right] = -\hbar \left[\frac{Q_{\mathrm{J}}}{-2e} + \frac{Q_{\mathrm{g}}}{-2e}\right]$, where Q_{J} and Q_{g} are the charges of the two capacitors. This is recognized as the number of Cooper pairs on the superconducting island in Fig. 1 times a constant $-\hbar$. Thus the eigenstates of $\hat{n}$ correspond to the number of Cooper pairs on the island. The quantization of charge on the superconducting island is the main idea behind the charge qubit, since the individual charge states can accurately become the eigenstates of the system in the limit $E_{\mathrm{C}} \gg E_{\mathrm{J}}$. The nonlinearity of the Josephson junction causes a nonzero anharmonicity [12], allowing the system to work as a qubit. The two lowest eigenstates and -energies can be controlled by changing n_{g}, which can be used for the implementation of logic gate operations [6].

2.3.3 Transmon qubit

In a transmon, an additional capacitor with capacitance C_{p} is added in parallel with the Josephson junction. The addition of the capacitor does not change the derivation of the Hamiltonian, since the additional capacitance is captured by the capacitance of the junction. The resulting Hamiltonian is identical to that in Eq. (38), except that $E_{\mathrm{C}} = \frac{e^2}{2(C_{\mathrm{J}} + C_{\mathrm{p}} + C_{\mathrm{g}})} = \frac{e^2}{2C_{\Sigma}}$. Thus the the effect of the additional capacitance is to lower the charging energy. To be more specific, the ratio $E_{\mathrm{J}}/E_{\mathrm{C}}$ is of the order of $\sim 10^2$ [10], in contrast to the low $E_{\mathrm{J}}/E_{\mathrm{C}} \approx 10^{-2}$ ratio of charge qubits [12]. The main advantage of the transmon design is that its energy is much less sensitive to voltage of charge drifts in the circuit than that of the charge qubit. The drawback of the high $E_{\mathrm{J}}/E_{\mathrm{C}}$ ratio is that the anharmonicity is weakened. However, this is not a major issue, since increasing the ratio $E_{\mathrm{J}}/E_{\mathrm{C}}$ decreases the sensitivity to charge drifts exponentially, whereas the anharmonicity weakens only algebraically. Thus the circuit still effectively works as a qubit [10].

Returning to the simple Hamiltonian in Eq. (38), in the limit $E_{\mathrm{J}}/E_{\mathrm{C}} \gg 1$ we can neglect the periodic boundary condition of φ and $\varphi + 2\pi$ being equal and expand the cosine in the Hamiltonian with a Taylor series $\cos\hat{\varphi} \approx 1 - \frac{1}{2}\hat{\varphi}^2 + \frac{1}{24}\hat{\varphi}^4$ [10]. Furthermore, due to the insensitivity to gate charge, we may set $n_{\mathrm{g}} = 0$ [10]. Thus

we arrive at a harmonic-oscillator Hamiltonian with a fourth-order anharmonic perturbation

$$\hat{H} \approx 4E_{\mathrm{C}}\hat{n}^2 + \frac{E_{\mathrm{J}}}{2}\hat{\varphi}^2 - \frac{E_{\mathrm{J}}}{24}\hat{\varphi}^4. \tag{39}$$

The harmonic part is brought to a different form using the annihilation and creation operators

$$4E_{\mathrm{C}}\hat{n}^2 + \frac{E_{\mathrm{J}}}{2}\hat{\varphi}^2 = \sqrt{8E_{\mathrm{C}}E_{\mathrm{J}}}(\hat{b}^\dagger\hat{b} + \frac{1}{2}), \tag{40}$$

where the operators $\hat{b}$ and $\hat{b}^\dagger$ are defined as

$$\hat{b} = -2\left(\frac{E_{\mathrm{C}}}{8E_{\mathrm{J}}}\right)^{\frac{1}{4}}\hat{n} + i\frac{1}{\sqrt{2}}\left(\frac{E_{\mathrm{J}}}{8E_{\mathrm{C}}}\right)^{\frac{1}{4}}\hat{\varphi}, \tag{41}$$

$$\hat{b}^\dagger = 2\left(\frac{E_{\mathrm{C}}}{8E_{\mathrm{J}}}\right)^{\frac{1}{4}}\hat{n} + i\frac{1}{\sqrt{2}}\left(\frac{E_{\mathrm{J}}}{8E_{\mathrm{C}}}\right)^{\frac{1}{4}}\hat{\varphi}. \tag{42}$$

By noticing that $\hat{\varphi} = -\frac{1}{\sqrt{2}}\left(\frac{8E_{\mathrm{C}}}{E_{\mathrm{J}}}\right)^{\frac{1}{4}}(\hat{b} + \hat{b}^\dagger)$, the Hamiltonian in Eq. (39) assumes the form

$$\hat{H} = \sqrt{8E_{\mathrm{C}}E_{\mathrm{J}}}\hat{b}^\dagger\hat{b} - \frac{E_{\mathrm{C}}}{12}(\hat{b} + \hat{b}^\dagger)^4, \tag{43}$$

where the constant energy term has been neglected. Transforming to the interaction picture with $H_0 = \sqrt{8E_{\mathrm{C}}E_{\mathrm{J}}}\hat{b}^\dagger\hat{b} = \omega_0\hat{b}^\dagger\hat{b}$, the annihilation operator becomes

$$
\begin{aligned}
\hat{b}_{\mathrm{I}} &\rightarrow e^{i\omega_0\hat{b}^\dagger\hat{b}t}\hat{b}e^{-i\omega_0\hat{b}^\dagger\hat{b}t} = e^{i\omega_0\hat{b}^\dagger\hat{b}t}\hat{b}\sum_{k=0}^{\infty}\frac{(-i)^k\omega_0^k(\hat{b}^\dagger\hat{b})^k}{k!} = e^{i\omega_0\hat{b}^\dagger\hat{b}t}\sum_{k=0}^{\infty}\frac{(-i)^k\omega_0^k\hat{b}(\hat{b}^\dagger\hat{b})^k}{k!}\\
&= e^{i\omega_0\hat{b}^\dagger\hat{b}t}\sum_{k=0}^{\infty}\frac{(-i)^k\omega_0^k(\hat{b}\hat{b}^\dagger)^k\hat{b}}{k!} = e^{i\omega_0\hat{b}^\dagger\hat{b}t}\sum_{k=0}^{\infty}\frac{(-i)^k\omega_0^k(\hat{b}^\dagger\hat{b}+1)^k}{k!}\hat{b}\\
&= e^{i\omega_0\hat{b}^\dagger\hat{b}t}e^{-i\omega_0(\hat{b}^\dagger\hat{b}+1)t}\hat{b} = e^{-i\omega_0 t}\hat{b},
\end{aligned} \tag{44}
$$

where we used the commutation relation $[\hat{b}, \hat{b}^\dagger] = 1$. Likewise, the operator $\hat{b}_{\mathrm{I}}^\dagger = e^{i\omega t}\hat{b}^\dagger$. The resulting interaction Hamiltonian is given by

$$\hat{H}_I = -\frac{E_{\mathrm{C}}}{12}(e^{-i\omega_0 t}\hat{b} + e^{i\omega_0 t}\hat{b}^\dagger)^4. \tag{45}$$

When expanding the above expression, one obtains sixteen different terms. The ones that have time dependence are those which have an uneven number of creation and annihilation operators, i.e., $e^{-2i\omega_0 t}\hat{b}\hat{b}\hat{b}^\dagger\hat{b}$. In the interaction picture, these terms are rotating with a very high frequency which causes their effects to average out on long timescales, allowing us to ignore them. This is also called the rotating-wave approximation [17]. Transforming back to the Schrödinger picture, six anharmonic terms of the sixteen that we started with are left in the Hamiltonian

$$\hat{H} = \sqrt{8E_{\mathrm{C}}E_{\mathrm{J}}}\hat{b}^\dagger\hat{b} - \frac{E_{\mathrm{C}}}{12}(\hat{b}^\dagger\hat{b}^\dagger\hat{b}\hat{b} + \hat{b}^\dagger\hat{b}\hat{b}^\dagger\hat{b} + \hat{b}^\dagger\hat{b}\hat{b}\hat{b}^\dagger + \hat{b}\hat{b}^\dagger\hat{b}^\dagger\hat{b} + \hat{b}\hat{b}^\dagger\hat{b}\hat{b}^\dagger + \hat{b}\hat{b}\hat{b}^\dagger\hat{b}^\dagger). \tag{46}$$

In appendix A, we show that the sum of the six terms is given in a more compact form as $-\frac{E_\text{C}}{4} - E_\text{C}\hat{b}^\dagger\hat{b} - \frac{E_\text{C}}{2}\hat{b}^\dagger\hat{b}^\dagger\hat{b}\hat{b}$. Neglecting the constant term, the Hamiltonian is brought in to the simple form

$$\hat{H} = (\sqrt{8E_\text{C}E_\text{J}} - E_\text{C})\hat{b}^\dagger\hat{b} - \frac{E_\text{C}}{2}\hat{b}^\dagger\hat{b}^\dagger\hat{b}\hat{b} \tag{47}$$

$$= \hbar\omega\hat{b}^\dagger\hat{b} + \frac{\hbar\alpha}{2}\hat{b}^\dagger\hat{b}^\dagger\hat{b}\hat{b}. \tag{48}$$

where the qubit frequency ω and anharmonicity α have also been defined.

3 Methods

In this section, we describe the method used to implement and characterize two-qubit gates.

3.1 Tunable coupling scheme

The system simulated in this work is based on Ref. [13], where the authors propose the use of an auxiliary qubit acting as a tunable coupler between the two logical qubits for implementing two-qubit gate operations. Figure 2 illustrates the system. The logical qubits effectively interact in two ways, by direct coupling between the qubits, and by an effective coupling through the auxiliary qubit, also referred to as the virtual exchange interaction. If the system parameters are set correctly, these two interactions cancel each other at an appropriate auxiliary qubit frequency, effectively decoupling the logical qubits. The advantage of the scheme is that the direct coupling is explicitly taken into account, and it is excluded from the sources of error. When the logical qubits are brought to resonance, an iSWAP gate can be carried out by tuning the frequency of the coupler.
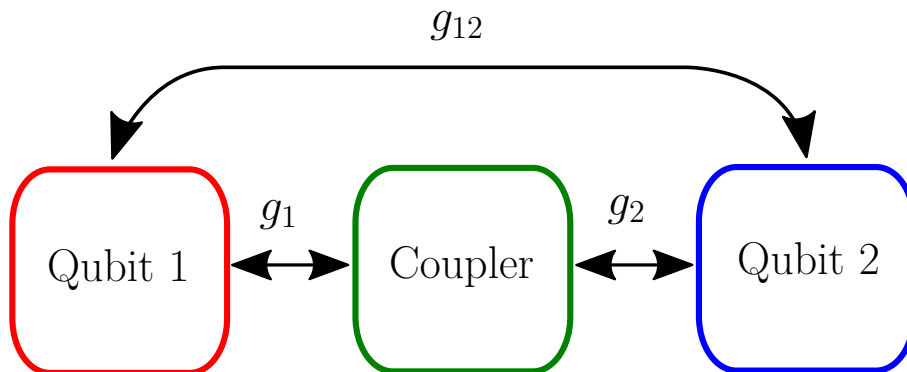

Figure 2: Schematic picture of the coupling scheme between Qubit 1 and Qubit 2. Here, g_1, g_2, and g_{12} are the coupling constants between the qubits.

Consider an ideal system consisting of three two-level systems with couplings between all of them, with a Hamiltonian given by

$$\hat{H}/\hbar = \sum_{j=1,2} \frac{1}{2}\omega_j \hat{\sigma}_j^z + \frac{1}{2}\omega_c \hat{\sigma}_c^z + g_{12}(\hat{\sigma}_1^+ \hat{\sigma}_2^- + \hat{\sigma}_1^- \hat{\sigma}_2^+) + \sum_{j=1,2} g_j(\hat{\sigma}_j^+ \hat{\sigma}_c^- + \hat{\sigma}_j^- \hat{\sigma}_c^+), \quad (49)$$

where ω_1, ω_c, and ω_2 denote the frequencies of the first logical qubit, the auxiliary coupler qubit, and the second logical qubit, respectively, whereas g_1 and g_2 are the coupling constants of Qubits 1 and 2 with the coupler and g_{12} is the direct coupling constant. The operators $\hat{\sigma}_k^z, \hat{\sigma}_k^+$, and $\hat{\sigma}_k^-$, $k \in \{1, c, 2\}$ are the Pauli-Z, raising, and lowering operators of each qubit, respectively. The full tensor product form of the operators has not been explicitly written down, such that for example the $\hat{\sigma}_z^c$ operator corresponds to the operator $\mathbb{1} \otimes \hat{\sigma}^z \otimes \mathbb{1}$ and $\hat{\sigma}_1^+$ corresponds to $\hat{\sigma}^+ \otimes \mathbb{1} \otimes \mathbb{1}$. The

states of the coupler are approximately decoupled from the other two qubits using the so-called Schrieffer–Wolff transformation,

$$\tilde{H} = e^{\hat{S}}\hat{H}e^{\hat{S}^\dagger}, \tag{50}$$

$$\hat{S} = \sum_{j=1,2} \frac{g_j}{\Delta_j}(\hat{\sigma}_j^+\hat{\sigma}_c^- - \hat{\sigma}_j^-\hat{\sigma}_c^+). \tag{51}$$

The Hamiltonian concerning the logical qubits transforms as

$$\begin{aligned}
\tilde{H}/\hbar &= \sum_{j=1,2} \frac{1}{2}\tilde{\omega}_j(\omega_c)\hat{\sigma}_j^z + \left(\frac{g_1 g_2}{\Delta(\omega_c)} + g_{12}\right)(\hat{\sigma}_1^+\hat{\sigma}_2^- + \hat{\sigma}_1^-\hat{\sigma}_2^+) \\
&= \sum_{j=1,2} \frac{1}{2}\tilde{\omega}_j(\omega_c)\hat{\sigma}_j^z + \tilde{g}(\omega_c)(\hat{\sigma}_1^+\hat{\sigma}_2^- + \hat{\sigma}_1^-\hat{\sigma}_2^+),
\end{aligned} \tag{52}$$

where it has been defined that $\frac{1}{\Delta(\omega_c)} = \left(\frac{1}{\Delta_1(\omega_c)} + \frac{1}{\Delta_2(\omega_c)}\right)/2$, $\Delta_j(\omega_c) = \omega_j - \omega_c$ and $\tilde{\omega}_j(\omega_c) = \omega_j + \frac{g_j^2}{\Delta_j(\omega_c)}$. All of the operators in Eq. (52) are transformed, even though they are denoted by the same symbols as before. The approximation holds if $g_j \ll |\Delta_j|$, that is, the coupling to the auxiliary qubit is dispersive. The description of the interaction between the two qubits is thus simplified into a direct effective coupling $\tilde{g}$. Assuming negative detunings from the coupler, $\Delta_j < 0$, the first term inside the expression for $\tilde{g}$ is negative, implying that it is possible to find a frequency ω_c^{off} such that $\tilde{g}(\omega_c^{\text{off}}) = 0$, thus fully decoupling the two qubits. Tuning ω_c away from ω_c^{off} turns on the interaction between the logical qubits, allowing the execution of logic gates.

If we choose $\omega_1 = \omega_2$, the iSWAP gate can be carried out. First we move into a frame rotating with qubit frequencies in the decoupled state, so that $\hat{H}_0/\hbar = \sum_{j=1,2} \frac{1}{2}\tilde{\omega}(\omega_c^{\text{off}})\hat{\sigma}_j^z$ and $\hat{H}_I(t)/\hbar = \sum_{j=1,2} \frac{1}{2}[\tilde{\omega}(t) - \tilde{\omega}(\omega_c^{\text{off}})]\hat{\sigma}_j^z + \tilde{g}(t)(\hat{\sigma}_1^+\hat{\sigma}_2^- + \hat{\sigma}_1^-\hat{\sigma}_2^+)$, where the possible time dependency of ω_c has been taken to account by the definitions $\tilde{\omega}(t) = \tilde{\omega}[\omega_c(t)]$ and $\tilde{g}(t) = \tilde{g}[\omega_c(t)]$. In this frame all state vectors stay constant with respect to time if $\omega_c = \omega_c^{\text{off}}$. It can be shown that $[\hat{H}_I(t_1), \hat{H}_I(t_2)] = 0$ for every t_1, t_2, and thus the time evolution operator of the system is $\hat{U}(t) = e^{-\frac{i}{\hbar}\int_0^t \hat{H}_I(t')\mathrm{d}t'}$ which we write in the basis formed of the combinations of the individual qubit eigenstates, $\{|00\rangle, |01\rangle, |10\rangle, |11\rangle\}$, where $|0\rangle$ is the ground state of an uncoupled qubit, as

$$\hat{U}(t) \cong \begin{bmatrix} e^{i\int_0^t[\tilde{\omega}(t') - \tilde{\omega}(\omega_c^{\text{off}})]\mathrm{d}t'} & 0 & 0 & 0 \\ 0 & \cos[\int_0^t \tilde{g}(t')\mathrm{d}t'] & -i\sin[\int_0^t \tilde{g}(t')\mathrm{d}t'] & 0 \\ 0 & -i\sin[\int_0^t \tilde{g}(t')\mathrm{d}t'] & \cos[\int_0^t \tilde{g}(t')\mathrm{d}t'] & 0 \\ 0 & 0 & 0 & e^{-i\int_0^t[\tilde{\omega}(t') - \tilde{\omega}(\omega_c^{\text{off}})]\mathrm{d}t'} \end{bmatrix}. \tag{53}$$

We observe that if $\int_0^t \tilde{g}[\omega_c(t')]\mathrm{d}t' = -\pi/2$, an iSWAP gate is introduced apart from the opposite phase factors on the states $|00\rangle$ and $|11\rangle$. The complete iSWAP modulo a global phase is realized by applying phase shift gates with an appropriate phase $\phi = \int_0^t \tilde{\omega}(t') - \tilde{\omega}(\omega_c^{\text{off}})\mathrm{d}t'$ on both of the qubits separately, resulting in the

transformation

$$\begin{bmatrix} 1 & 0 \\ 0 & e^{i\phi} \end{bmatrix} \otimes \begin{bmatrix} 1 & 0 \\ 0 & e^{i\phi} \end{bmatrix} = e^{i\phi} \begin{bmatrix} e^{-i\phi} & 0 & 0 & 0 \\ 0 & 1 & 0 & 0 \\ 0 & 0 & 1 & 0 \\ 0 & 0 & 0 & e^{i\phi} \end{bmatrix}. \tag{54}$$

A useful, alternative approach is to consider the symmetric and antisymmetric eigenstates $|s\rangle = ((|01\rangle + |10\rangle)/\sqrt{2}$ and $|a\rangle = (|01\rangle - |10\rangle)/\sqrt{2}$ with eigenenergies $E_{\mathrm{s}}/\hbar = \tilde{g}$ and $E_{\mathrm{a}}/\hbar = -\tilde{g}$, respectively. The temporal evolution of an arbitrary combination of states $|01\rangle$ and $|10\rangle$ with constant $\tilde{\omega}$ and $\tilde{g}$ is given by

$$\hat{U}(t)(a|01\rangle + b|10\rangle) = a(e^{-i\tilde{g}t}|s\rangle + e^{i\tilde{g}t}|a\rangle)/\sqrt{2} + b(e^{-i\tilde{g}t}|s\rangle - e^{i\tilde{g}t}|a\rangle)/\sqrt{2} \tag{55}$$

$$= |01\rangle \left[(e^{-i\tilde{g}t} + e^{i\tilde{g}t})a + (e^{-i\tilde{g}t} - e^{i\tilde{g}t})b \right]/2$$

$$+ |10\rangle \left[(e^{-i\tilde{g}t} - e^{i\tilde{g}t})a + (e^{i\tilde{g}t} + e^{-i\tilde{g}t})b \right]/2 \tag{56}$$

$$= |01\rangle \left[a\cos(\tilde{g}t) - bi\sin(\tilde{g}t) \right] + |01\rangle \left[-ai\sin(\tilde{g}t) + b\cos(\tilde{g}t) \right], \tag{57}$$

which again produces the iSWAP operation for $\int_0^t \tilde{g}[\omega_{\mathrm{c}}(t')]\mathrm{d}t' = \tilde{g}t = -\pi/2$. Thus, the swapping is mediated by the two eigenstates $|s\rangle$ and $|a\rangle$, with the interaction strength connected to their eigenenergies by $\tilde{g} = (E_{\mathrm{s}} - E_{\mathrm{a}})/(2\hbar)$.

3.2 Simulated system

As an implementation of the coupling scheme presented in Sec. 3.1, we consider a system of three flux-tunable transmon qubits capacitively coupled to each other. The circuit diagram of the system and the relevant definitions are given in Fig. 3. Single Josephson junctions have been replaced by two parallel junctions in the transmons. As magnetic flux is applied through the thus formed loops, the resulting components behave essentially as single Josephson junctions with magnetic-flux tunable Josephson energies, making the resonance frequencies of the qubits tunable as well. The circuit is quantized by choosing $\varphi_\lambda, \lambda \in \{1, c, 2\}$ as the generalized coordinates and applying identical steps to those used in deriving the transmon Hamiltonian in Sec. 2.3, resulting in the Hamiltonian operator

$$\hat{H} = \hat{H}_1 + \hat{H}_{\mathrm{c}} + \hat{H}_2 + \hat{H}_{1\mathrm{c}} + \hat{H}_{2\mathrm{c}} + \hat{H}_{12}, \tag{58}$$

$$\hat{H}_\lambda/\hbar = \omega_\lambda \hat{b}_\lambda^\dagger \hat{b}_\lambda + \frac{\alpha_\lambda}{2} \hat{b}_\lambda^\dagger \hat{b}_\lambda^\dagger \hat{b}_\lambda \hat{b}_\lambda, \quad \lambda \in \{1, c, 2\}, \tag{59}$$

$$\hat{H}_{j\mathrm{c}}/\hbar = g_j(\hat{b}_j^\dagger \hat{b}_{\mathrm{c}} + \hat{b}_j \hat{b}_{\mathrm{c}}^\dagger - \hat{b}_j^\dagger \hat{b}_{\mathrm{c}}^\dagger - \hat{b}_j \hat{b}_{\mathrm{c}}), \quad j \in \{1, 2\}, \tag{60}$$

$$\hat{H}_{12}/\hbar = g_{12}(\hat{b}_1^\dagger \hat{b}_2 + \hat{b}_1 \hat{b}_2^\dagger), \tag{61}$$

where $\hat{b}_\lambda^\dagger$ and $\hat{b}_\lambda$ are the creation and annihilation operators for qubit λ. The full tensor product forms have been not been explicitly expressed, and for example $\hat{b}_2 = \mathbb{1} \otimes \mathbb{1} \otimes \hat{b}$ and $\hat{b}_{\mathrm{c}}^\dagger = \mathbb{1} \otimes \hat{b}^\dagger \otimes \mathbb{1}$. In the simulations, $\hat{H}$ was cut off at five energy levels per qubit so that the simulated operator was in practise a 125×125 matrix.
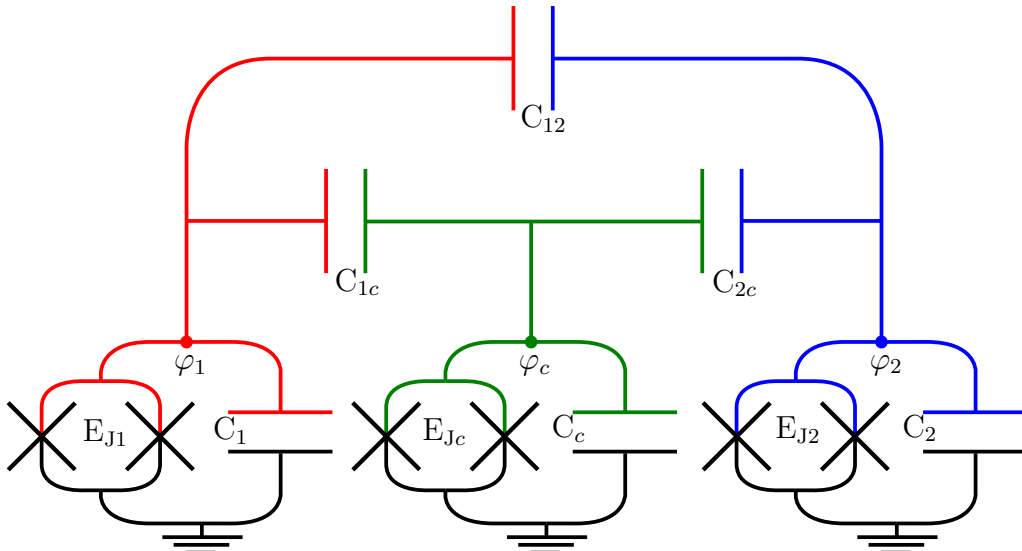
Figure 3: Simulated system of three capacitively coupled transmon qubits. Differently colored regions show the different superconducting islands. The auxiliary qubit is in the center and the logical qubits are on the sides.

The angular frequencies ω_λ, anharmonicities α_λ, and the coupling constants g_j and g_{12} are given by

$$\omega_\lambda = (\sqrt{8E_{J\lambda}E_{C\lambda}} - E_{C\lambda})/\hbar, \tag{62}$$

$$\alpha_\lambda = -E_{C\lambda}/\hbar, \tag{63}$$

$$g_j = \frac{1}{2}\frac{C_{jc}}{\sqrt{C_jC_c}\hbar}\sqrt{\omega_j\omega_c}, \tag{64}$$

$$g_{12} = \frac{1}{2}(1+\eta)\frac{C_{12}}{\sqrt{C_1C_2}\hbar}\sqrt{\omega_1\omega_2}, \tag{65}$$

where $\eta = \frac{C_{1c}C_{2c}}{C_{12}C_c}$ and $E_{C\lambda} = \frac{e^2}{2C_\lambda}$. The constants have been renormalized by assuming that $C_{12} \ll C_{jc} \ll C_\lambda$ where $j, \lambda \in \{1, 2\}$. In an experimental realization, this does not pose any problems since the required parameters are obtained by direct measurements rather than from Eqs. (62)–(65). In this thesis, the basis states of the simulation are consistently ordered as Qubit 1, the coupler, Qubit 2. For example, $|001\rangle = |0\rangle \otimes |0\rangle \otimes |1\rangle$ denotes the state where the Qubit 1 and the coupler are in the ground state and Qubit 2 is in the excited state, with $|0\rangle$ and $|1\rangle$ being the ground and excited state for an uncoupled qubit. As in the theoretical model presented in Sec. 3.1, the Hamiltonian is approximately transformed such that the auxiliary qubit is decoupled from Qubits 1 and 2 using a Schrieffer-Wolff transformation presented in Eq. (50) with $\hat{S} = \sum_{j=1,2}\left[\frac{g_j}{\Delta_j}(\hat{b}_j^\dagger\hat{b}_c - \hat{b}_j\hat{b}_c^\dagger) - \frac{g_j}{\Sigma_j}(\hat{b}_j^\dagger\hat{b}_c^\dagger - \hat{b}_j\hat{b}_c)\right]$. Here $\Delta_j(\omega_c) = \omega_j - \omega_c$ and $\Sigma_j(\omega_c) = \omega_j + \omega_c$. This results in a Hamiltonian corresponding to the one in Eq. (52), with an effective interaction strength $\tilde{g}$ between the qubits

$$\tilde{H}/\hbar = \sum_{j=1,2}\left(\tilde{\omega}_j\hat{b}_j^\dagger\hat{b}_j + \frac{\tilde{\alpha}_j}{2}\hat{b}_j^\dagger\hat{b}_j^\dagger\hat{b}_j\hat{b}_j\right) + \tilde{g}(\hat{b}_1^\dagger\hat{b}_2 + \hat{b}_1\hat{b}_2^\dagger). \tag{66}$$

The values of $\tilde{g}, \tilde{\omega}_j$ and $\tilde{\alpha}_j$ are given by

$$\tilde{g}(\omega_c) \approx \frac{1}{2\hbar} \left(\frac{\omega_c}{2\Delta(\omega_c)} \eta - \frac{\omega_c}{2\Sigma(\omega_c)} \eta + \eta + 1 \right) \frac{C_{12}}{C_1 C_2} \sqrt{\omega_1 \omega_2}, \tag{67}$$

$$\tilde{\omega}_j(\omega_c) \approx \omega_j + \frac{g_1^2}{\hbar} \left(\frac{1}{\Delta_j(\omega_c)} - \frac{1}{\Sigma_j(\omega_c)} \right), \tag{68}$$

$$\tilde{\alpha}_j \approx \alpha_j, \tag{69}$$

where $\frac{1}{\Delta(\omega_c)} = (\frac{1}{\Delta_1(\omega_c)} + \frac{1}{\Delta_2(\omega_c)})/2$ and $\frac{1}{\Sigma(\omega_c)} = (\frac{1}{\Sigma_1(\omega_c)} + \frac{1}{\Sigma_2(\omega_c)})/2$. In addition to assuming that $g_j \ll |\Delta_j|$, we also assume that the anharmonicities α_j are small in using the transformation. If we consider only the first two energy levels of each qubit, that is, approximate them to be actual two-state systems, Eq. (66) becomes essentially identical to Eq. (52). Thus we expect the results of Sec. 3.1 to hold to some degree also for the non-ideal system, and in the case $\omega = \omega_1 = \omega_2$ an iSWAP gate should be able implementable.

3.3 Numerical simulation of the system

3.3.1 Computational states and the effective interaction strength

A number of practical concerns should be addressed for the simulations. The first is the problem of which states to define as the computational basis states corresponding to the ideal two-qubit states $|00\rangle, |01\rangle, |10\rangle$, and $|11\rangle$. The used states are the eigenstates of the entire system in the decoupled state $\omega_c = \omega_c^{\text{off}}$ that match closely with the tensor product combinations of the uncoupled qubit eigenstates, $|000\rangle, |001\rangle, |100\rangle$, and $|101\rangle$. These states are labeled as $\widetilde{|000\rangle}, \widetilde{|001\rangle}, \widetilde{|100\rangle}$, and $\widetilde{|101\rangle}$. According to the two-level theory of Sec. 3.1, these matching eigenstates should exist as in the case that $\omega_c = \omega_c^{\text{off}}$, $|00\rangle, |01\rangle, |10\rangle$ and $|11\rangle$ are precisely eigenstates of the system. Other eigenstates with ω_c at the decoupling frequency that correspond closely to some state formed of the uncoupled qubit eigenstates are referred to with the same convention as the computational states, so that the state $\widetilde{|010\rangle}$ corresponds to an eigenstate that is close, but not equal to, $|010\rangle = |0\rangle \otimes |1\rangle \otimes |0\rangle$.

Instead of using the analytical formula for the effective interaction strength in Eq. (67), we use a more accurate method utilizing the numerically calculated eigenenergies of the system. We note that the swapping operation in the theory of Sec. 3.1 is mediated by the symmetric and antisymmetric combinations of the computational states $|01\rangle$ and $|10\rangle$. This fact is translated to the simulated system by noting that when $\omega_c \approx \omega_c^{\text{off}}$, there should exist two eigenstates close to states $\widetilde{|001\rangle} + \widetilde{|100\rangle}$ and $\widetilde{|001\rangle} - \widetilde{|100\rangle}$ with eigenenergies E_s and E_a. Thus, as in Sec. 3.1, an effective interaction strength $\tilde{g}_e$ is calculated as

$$\tilde{g}_e = (E_s - E_a)/(2\hbar). \tag{70}$$

By finding the zero of $\tilde{g}_e$ with respect to ω_c, the decoupling frequency ω_c^{off} is found and consequently the computational states $\widetilde{|000\rangle}, \widetilde{|001\rangle}, \widetilde{|100\rangle}$, and $\widetilde{|101\rangle}$ are defined as the eigenstates at $\omega_c = \omega_c^{\text{off}}$.

When calculating an optimal pulse shape using $\tilde{g}_e$, its interpretation is slightly different for non-adiabatic and adiabatic pulse shapes. In the case of a non-adiabatic pulse, for instance a square pulse where ω_c is tuned instantaneously away from ω_c^{off} until the end of the pulse, the temporal evolution is governed by the projection of the starting state to the new eigenstates of the system. At small deviations away from ω_c^{off}, however, there exist eigenstates close to $\widetilde{|001\rangle} + \widetilde{|100\rangle}$ and $\widetilde{|001\rangle} - \widetilde{|100\rangle}$ and the evolution is approximately the simple swapping mediated by these eigenstates. In the case of a pulse causing an adiabatic change in the system it only matters that the eigenstates at the end of the pulse are close to the symmetric and antisymmetric combinations of $\widetilde{|001\rangle}$ and $\widetilde{|100\rangle}$. In both cases, however, the condition $\int_0^T \tilde{g}_e(t)\mathrm{d}t = -\pi/2$ results in the optimal swapping operation. This is discussed in more detail in Appendix B.

3.3.2 Used rotating frame

We carry out the simulations in a rotating frame where the states $\widetilde{|001\rangle}$ and $\widetilde{|100\rangle}$ are time-independent. Specifically, the bare Hamiltonian is chosen as $\hat{H}_0 = E_{\widetilde{|001\rangle}}(\hat{b}_1^\dagger \hat{b}_1 + \hat{b}_c^\dagger \hat{b}_c + \hat{b}_2^\dagger \hat{b}_2)$, where $E_{\widetilde{|001\rangle}}$ is the eigenenergy of states $\widetilde{|001\rangle}$ and $\widetilde{|100\rangle}$. The simulated interaction Hamiltonian is given by

$$\hat{H}_I = \hat{H}_{1,I} + \hat{H}_{c,I} + \hat{H}_{2,I} + \hat{H}_{1c,I} + \hat{H}_{2c,I} + \hat{H}_{12,I} \tag{71}$$

$$\hat{H}_{\lambda,I}/\hbar = (\omega_\lambda - E_{\widetilde{|001\rangle}})\hat{b}_\lambda^\dagger \hat{b}_\lambda + \frac{\alpha_\lambda}{2}\hat{b}_\lambda^\dagger \hat{b}_\lambda^\dagger \hat{b}_\lambda \hat{b}_\lambda, \lambda \in \{1, c, 2\} \tag{72}$$

$$\hat{H}_{jc,I}/\hbar = g_j(\hat{b}_j^\dagger \hat{b}_c + \hat{b}_j \hat{b}_c^\dagger - e^{2\frac{i}{\hbar}E_{\widetilde{|001\rangle}}t}\hat{b}_j^\dagger \hat{b}_c^\dagger - e^{-2\frac{i}{\hbar}E_{\widetilde{|001\rangle}}t}\hat{b}_j \hat{b}_c), j \in \{1, 2\} \tag{73}$$

$$\hat{H}_{12,I}/\hbar = g_{12}(\hat{b}_1^\dagger \hat{b}_2 + \hat{b}_1 \hat{b}_2^\dagger). \tag{74}$$

Note that in general, the coupling factors g_1 and g_2 depend on time since they are functions of the time-controllable parameter ω_c. Also note that unlike in the approximated ideal model presented in Sec. 3.1, even in this rotating frame, not all computational states stay completely unchanged with respect to time since the spacing between $E_{\widetilde{|000\rangle}}$, $E_{\widetilde{|001\rangle}}$ and $E_{\widetilde{|101\rangle}}$ is not exactly even. Thus some of the computational states in a rotating frame with $\hat{H}_0$ of a harmonic oscillator type have to get phase-shifted even when $\omega_c = \omega_c^{\text{off}}$.

3.3.3 Gate error

To estimate the error of a physical implementation of a logic gate we define the fidelity as

$$f(|\psi_1\rangle, |\psi_2\rangle) = |\langle\psi_1|\psi_2\rangle|^2, \tag{75}$$

for some states $|\psi_1\rangle$ and $|\psi_2\rangle$. It can be interpreted as the overlap between the two states. If $|\psi_{\text{ideal}}\rangle$ is the desired ideal state after a computational process starting from some fixed input state, the error related to an actual state $|\psi\rangle$ after the process is then

$$\varepsilon = 1 - f(|\psi_{\text{ideal}}\rangle, |\psi\rangle) = 1 - |\langle\psi_{\text{ideal}}|\psi\rangle|^2. \tag{76}$$

The error of the gate operation is quantified by calculating the average fidelity of the resulting states from a set of 16 input states. Specifically, we choose the set of the 16 states that correspond to all tensor product combinations of the states $|0\rangle, |1\rangle, \frac{1}{\sqrt{2}}(|0\rangle + |1\rangle)$ and $\frac{1}{\sqrt{2}}(|0\rangle + i|1\rangle)$ [18].

Since the error given by the fidelity is not useful in identifying the cause of the error, a simple scheme for comparing the errors arising from different states is used. Let us assume that the states $|1\rangle, |2\rangle, |3\rangle \dots$ form an orthonormal basis in the Hilbert space. The fidelity of a state $|\psi\rangle$ compared with the ideal final state $|\psi_{\text{ideal}}\rangle$ expands as

$$| \langle \psi_{\text{ideal}} | \psi \rangle |^2 = \left| \sum_{k=1}^{N} \langle \psi_{\text{ideal}} | k \rangle \langle k | \psi \rangle \right|^2, \tag{77}$$

where N is the dimension of the Hilbert space. The part of the fidelity caused by the coefficient of $|\psi\rangle$ along $|k\rangle$ is then associated with the term $\langle \psi_{\text{ideal}} | k \rangle \langle k | \psi \rangle$. If the gate operation was perfect, the fidelity would equal to 1 and the term associated with the coefficient of $|\psi\rangle$ along $|k\rangle$ would be $\langle \psi_{\text{ideal}} | k \rangle \langle k | \psi_{\text{ideal}} \rangle$. Thus the error related to state $|k\rangle$ is defined as

$$\epsilon_{\text{n}} = \left| | \langle \psi_{\text{ideal}} | k \rangle \langle k | \psi_{\text{ideal}} \rangle |^2 - | \langle \psi_{\text{ideal}} | k \rangle \langle k | \psi \rangle |^2 \right|, \tag{78}$$

where the terms have been squared so that the magnitude of the expression matches with the error calculated from the fidelity.

3.3.4 Correction of the phase shift on computational states

The problem of the individual qubits rotating during the iSWAP gate discussed in Sec. 3.1 has to be also addressed. In the following sections, the errors/fidelities are presented with the assumption that an appropriate phase shift is applied to the qubits after the simulated interaction. In practice, since the computational states are not simply the tensor product combinations of the uncoupled qubit eigenstates $|0\rangle$ and $|1\rangle$, this is implemented by finding the fidelity-optimizing phase of states $|000\rangle$ and $|101\rangle$. The exact mechanics of the phase shift gate are not considered in this thesis. Consequently, the accuracy of such a transformation and the time taken for it are not accounted for in the results. For slightly better results, it would be possible to rotate each qubit by some amounts ϕ_1 and ϕ_2, but this would also necessarily cause a phase shift between states $|001\rangle$ and $|100\rangle$ and increase the time needed for the global optimization routine. Since the error of the gate operation is calculated using the mean fidelity of the 16 input states, the optimization is not actually calculated for each state fidelity, but for the mean fidelity. This is because in an actual quantum computer the correction to the phases should be predetermined, as it is not possible to know the input states in advance.

The simulations were carried out using a quantum mechanics simulation library for Python, Qutip 4 [19].

4 Results

In this section, we present the results from our numerical simulations of the iSWAP gate using a tunable coupler and compare these results to the analytic results in Secs. 3.1 and 3.3. In Table 1 we list all of the essential parameters used in the simulation as well as the ω_c^{off} solved from $\tilde{g}_e$ for these parameters. Since the parameters, in particular the frequencies, concerning qubits 1 and 2 are chosen to be symmetric for the iSWAP gate, they will be referred to with a common label $\omega = \omega_1 = \omega_2$ for the rest of this thesis.

$\omega_1/2\pi$	$\omega_2/2\pi$	$\omega_c^{\text{off}}/2\pi$	C_1	C_c	C_2	C_{1c}	C_{2c}	C_{12}
4GHz	4Ghz	5.362GHz	70fF	200fF	70fF	4fF	4fF	0.1fF

Table 1: Parameters used in the simulation and the value of the decoupling frequency ω_c^{off}

4.1 Qualitative behaviour of the system

Figure 4(a) shows the numerically obtained effective coupling strength $\tilde{g}_e$ as well as its analytical counterpart from Eq. (67). With the coupler frequency close to ω_c^{off} the two approaches agree well, which is not surprising since Eq. (67) assumes that $|\omega_c - \omega_c^{\text{off}}| \ll 0$. With ω_c approaching ω, however, the analytical result starts to diverge from the numerically calculated value. Figures 4(b)–(d) show visualizations of three eigenstates relevant to the swapping process as functions of studied ω_c. Two features are pointed out: Firstly, all of the eigenstates are almost entirely inside the subspace spanned by the basis states $\widetilde{|001\rangle}, \widetilde{|100\rangle}$, and $\widetilde{|010\rangle}$ for all ω_c. Equivalently, any state vector inside this subspace can be formed by these three eigenstates and the temporal evolution is determined by them. Secondly, we observe that for $\omega_c \approx \omega_c^{\text{off}}$, there exist two eigenstates that are very close to the states $\widetilde{|001\rangle} + \widetilde{|100\rangle}$ and $\widetilde{|001\rangle} - \widetilde{|100\rangle}$, as it should be. For ω_c close to ω, however, the purely symmetric eigenstate disappears and is in general replaced by a state of the form $a(\widetilde{|001\rangle} + \widetilde{|100\rangle}) - \sqrt{1 - 2a^2}\widetilde{|010\rangle}$, whereas the state that is $\widetilde{|010\rangle}$ for $\omega_c = \omega_c^{\text{off}}$ is replaced by a state $b(\widetilde{|001\rangle} + \widetilde{|100\rangle}) + \sqrt{1 - 2b^2}\widetilde{|010\rangle}$.

Figure 5 shows an example temporal evolution of the computational states for a square pulse. The gate duration is chosen to be 100 ns and the condition $\int_0^T \tilde{g}_e(t)\mathrm{d}t = -\pi/2$ results in the coupler frequency $\omega_c/2\pi \approx 4.768$GHz. It is observed from Fig. 4(b) that at this coupler frequency there exists an eigenstate close to $\widetilde{|001\rangle} + \widetilde{|100\rangle}$, implying that the swapping interaction should be close to ideal. In Fig. 5, the phases of the states $\widetilde{|000\rangle}$ and $\widetilde{|101\rangle}$ have also been corrected with the method explained in Sec. 3.3.4. Clearly, swapping takes place between the states $\widetilde{|001\rangle}$ and $\widetilde{|100\rangle}$, while nothing except equally large phase shifts are imposed on states $\widetilde{|000\rangle}$ and $\widetilde{|101\rangle}$. Ignoring the global phase picked up during the gate operation, at least on a qualitative level the iSWAP operation is completed successfully.
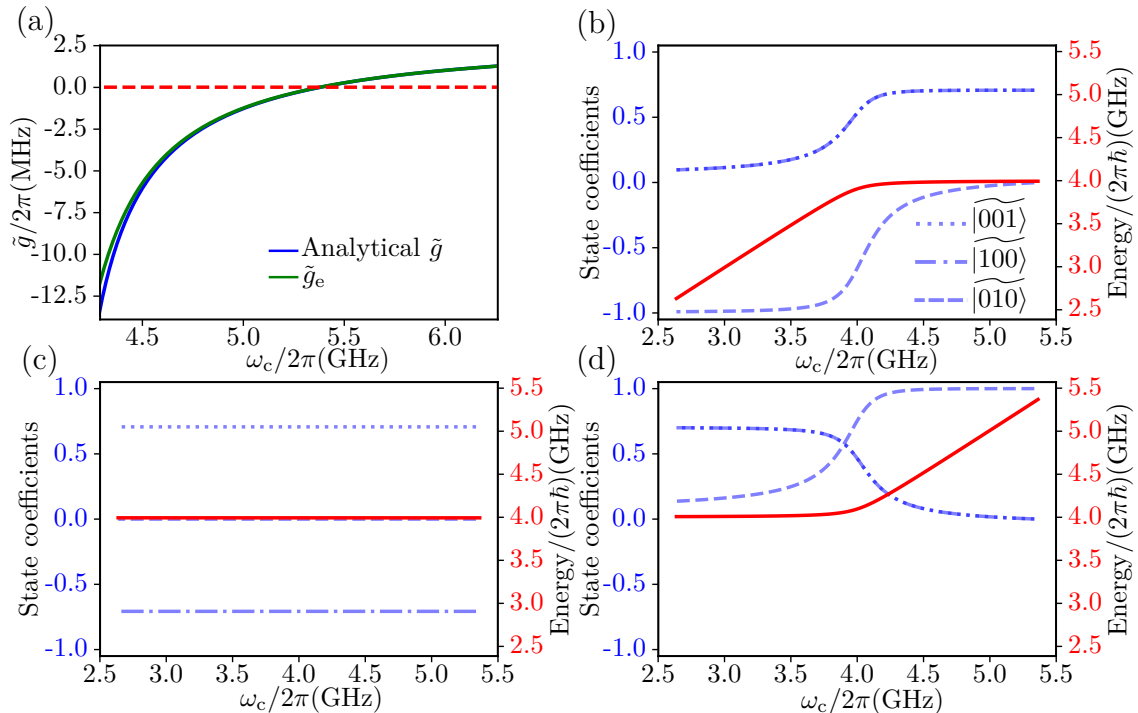
Figure 4: (a) Effective interaction strength between Qubits 1 and 2 calculated numerically (green line) and according to Eq. (67) (blue line) as functions of the frequency of the auxiliary qubit. (b)–(d) Eigenstates relevant to the swapping interaction represented as the coefficients of the projections onto the states $\widetilde{|001\rangle}$(dotted line), $\widetilde{|100\rangle}$(dash-dotted line), and $\widetilde{|010\rangle}$(dashed line) as functions of ω_c. The energies of the states are shown by the red line. The squared sum of the three coefficients squared is at its minimum at about 0.99999993, implying that the eigenstates are almost entirely within the subspace spanned by the states $\widetilde{|001\rangle}$, $\widetilde{|001\rangle}$ and $\widetilde{|010\rangle}$. For high ω_c, the computed eigenstates correspond to the states $\widetilde{|s\rangle} = \widetilde{|001\rangle} + \widetilde{|100\rangle}$, $\widetilde{|a\rangle} = \widetilde{|100\rangle} - \widetilde{|001\rangle}$, and $\widetilde{|010\rangle}$, for panels (b),(c), and (d), respectively. In (b) and (d), the coefficients of $\widetilde{|001\rangle}$ and $\widetilde{|100\rangle}$ overlap everywhere.

4.2 Gate error

To obtain a more complete picture of the performance of the system, the gate error for a range of different coupler frequencies using a square pulse and times ranging from 0 to 100 ns is shown in Fig. 6(a). The gate error is calculated as explained in Sec.3.3.3. We show also the best pulse durations for different ω_c predicted by the analytical $\tilde{g}$ and $\tilde{g}_e$ calculated from the eigenenergies as well as the lowest errors searched from the data set. Near ω_c^{off}, at long gate durations, the error evolves in time as expected, by smoothly decreasing until the swapping operation has happened and then increasing. As $\omega_c \to \omega$, however, a somewhat complicated pattern appears where the fidelity oscillates fast with several frequencies. This pattern is explained in part with the strong coupling to the state $\widetilde{|010\rangle}$ which results in an oscillation in the coefficients of states $\widetilde{|001\rangle}$ and $\widetilde{|100\rangle}$ with two overlapping frequencies. This is studied in Appendix C by taking in to account the three eigenstates in Fig. 4 in calculating the temporal evolution. Figure 6(b) presents a magnified view, where
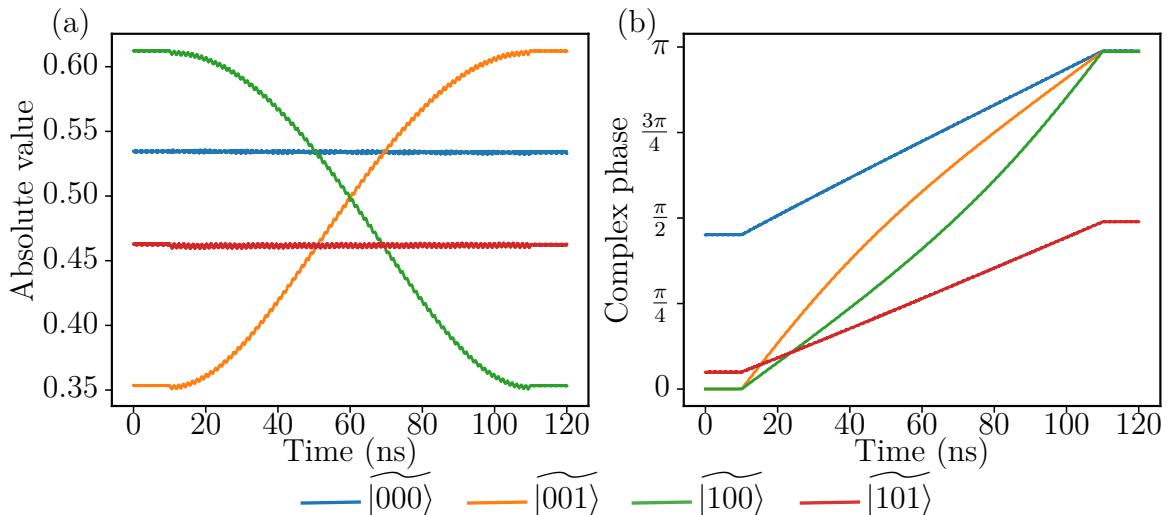
Figure 5: Evolution of the input state $i\sqrt{\frac{2}{7}}\widetilde{|000\rangle} + \frac{1}{\sqrt{8}}\widetilde{|001\rangle} + \sqrt{\frac{3}{8}}\widetilde{|100\rangle} + \sqrt{\frac{3}{14}}\widetilde{|101\rangle}$ for a square pulse of ω_c from ω_c^{off} to $2\pi\times4.768$ GHz. (a) The absolute values of the coefficients of each computational state. (b) The complex phases of the coefficients of the computational states. Optimal phase shift gates have been applied for all different times, showing the evolution to the final iSWAP state smoothly. This also causes the phases corresponding to the states $\widetilde{|000\rangle}$ and $\widetilde{|101\rangle}$ in panel (b) not to start exactly at $\pi/2$ and 0, respectively, since the optimizer finds a state slightly closer to the ideal final state using a small phase shift. The iSWAP gate is produced apart from a global phase shift, as the end state is approximately $e^{i\pi/2}(i\sqrt{\frac{2}{7}}\widetilde{|000\rangle} + i\sqrt{\frac{3}{8}}\widetilde{|001\rangle} + i\frac{1}{\sqrt{8}}\widetilde{|100\rangle} + \sqrt{\frac{3}{14}}\widetilde{|101\rangle})$.

it is visible that the prediction of the numerically calculated $\tilde{g}_e$ does indeed match better with the searched best fidelities than the one by the analytical $\tilde{g}$.

Since the coupling strength $\tilde{g}_e$ gives better predictions for the length of the pulse than the analytical result of Eq. (67), it is meaningful to ask how well exactly does the prediction match with the actual optimal fidelity for a given gate duration. The gate errors with different pulse durations and amplitudes calculated from $\int_0^T \tilde{g}_e(t)\mathrm{d}t = -\pi/2$ are shown in Fig. 7 with the minimum errors searched from Fig. 6. Comparison of the predicted and the actual best square pulse errors reveal that the predicted pulse error meets the searched error for some specific gate durations, otherwise oscillating at higher values. Both of the errors decrease with increasing gate duration as they should, but after about 60 ns the rate of the decrease slows down. To study if the error can be further decreased by making the pulse adiabatic, simulation results with pulse lengths and amplitudes predicted by $\tilde{g}_e$ are also shown with two other pulse shapes. These are the sine pulse, i.e., a modulation on the coupler frequency of the form $\omega_c(t) = \omega_c^{\text{off}}[1 - A\sin(\frac{\pi}{T}t)]$ and a sine squared pulse, where the coupler frequency varies as $\omega_c(t) = \omega_c^{\text{off}}[1 - A\sin^2(\frac{\pi}{T}t)]$. Here, A is a constant. At short pulse durations the sine pulse yields higher errors than the square pulse, but approximately at 34 ns the error decreases below the best possible square pulse and reaches a value below 10^{-5} at about 100 ns. In contrast to the predicted square pulse, the fidelity increases smoothly. The sine squared pulse, on the other
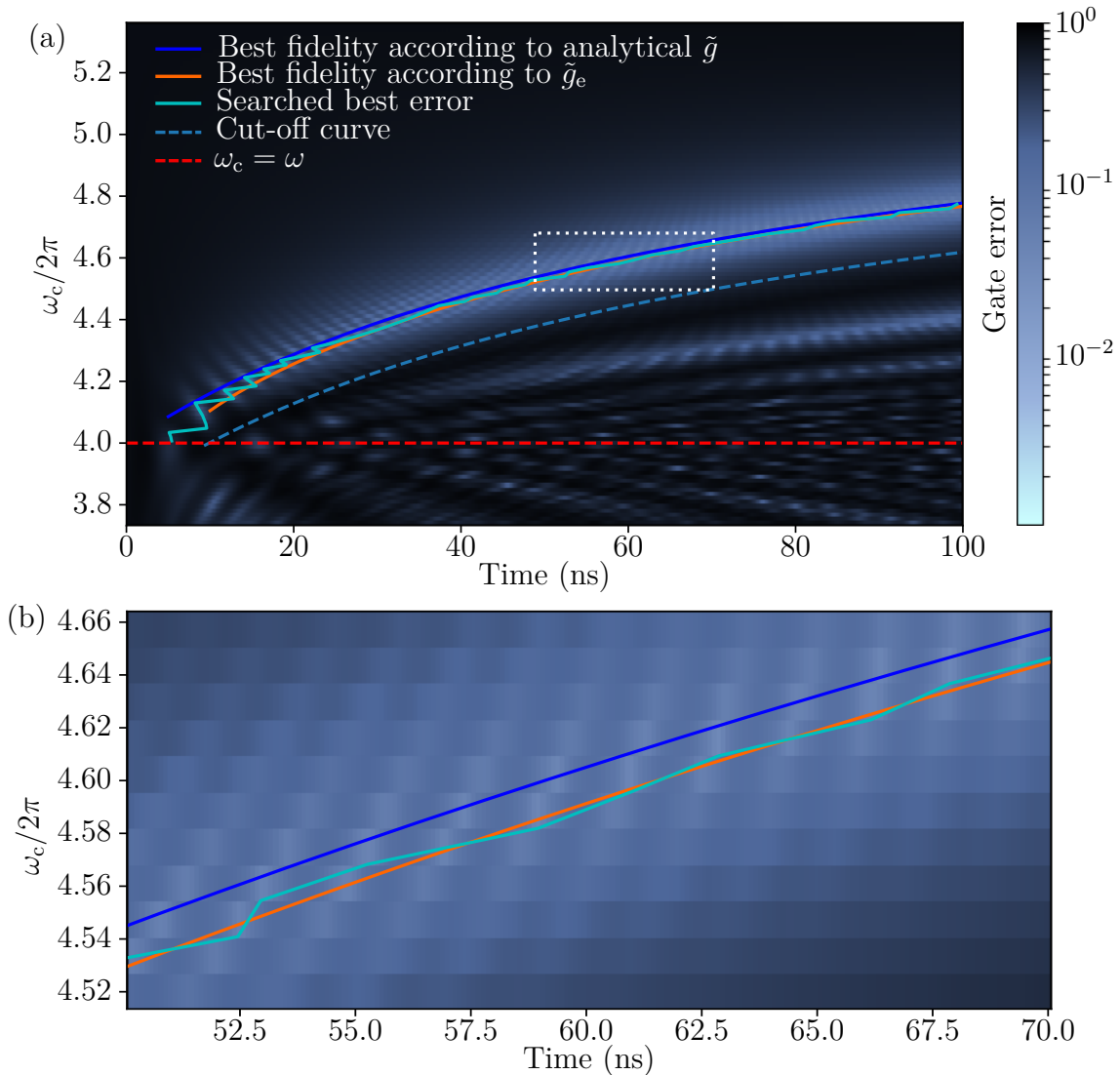
Figure 6: (a) Error of the gate operation as a function of gate duration and coupler frequency during a square pulse. We show as indicated the optimal gate durations for different frequencies calculated with the analytical $\tilde{g}$ from Eq. (67) and $\tilde{g}_e$, as well as a curve showing the best possible fidelity for different values of ω_c searched from the simulation results. The search is carried out left of the cut-off curve. (b) Magnification of panel (a) in the area indicated by the rectangle.

hand, while producing better fidelities than the square pulse at long gate durations, yields consistently higher errors than the sine pulse.

4.3 Analysis of error sources

Two questions arise: What causes the different pulse shapes to exhibit different errors and which computational states cause the most error? Figure 8(a) shows the evolution of the average gate error during a single gate operation for the different control pulses. The error of the sine and sine squared pulses decrease smoothly, while
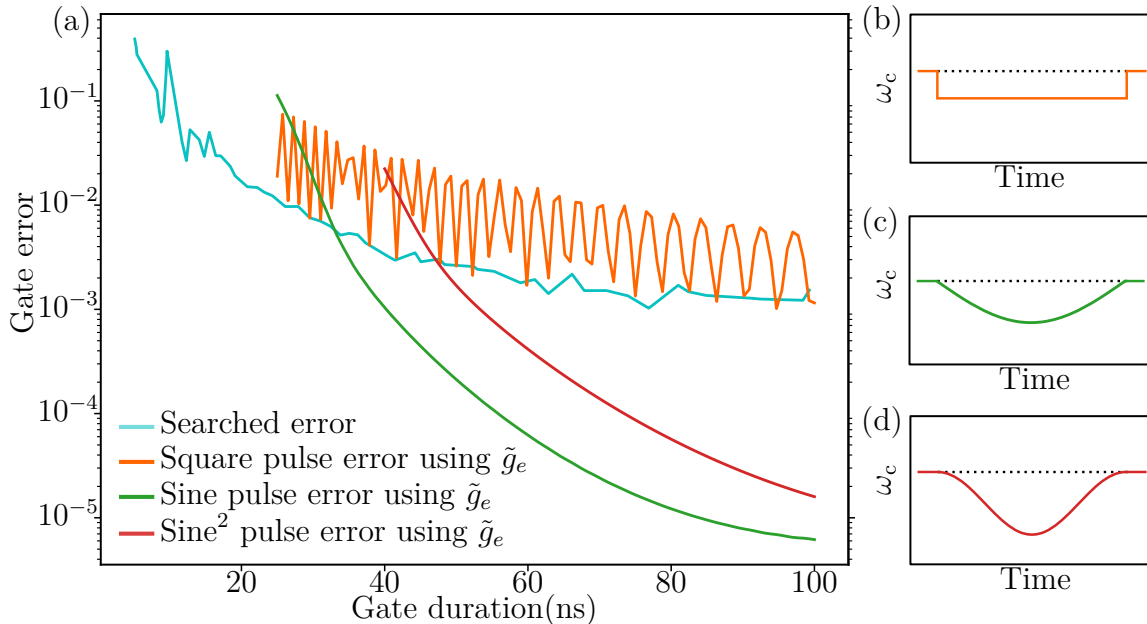
Figure 7: (a) Minimum errors for a square pulse searched from Fig. 6(a) and errors from the best pulse amplitude-duration combinations for square, sine, and sine squared pulse shapes according to $\int_0^t \tilde{g}_e(t)dt = -\pi/2$ as functions of the gate duration. (b)–(d) Illustrations of the different pulse shapes, with square pulse in (b), sine pulse in (c), and sine squared in (d).

the error of the square pulse begins to oscillate at the end of the gate operation. The error related to the different computational states according to Eq. (78) for the square pulse is presented in Fig. 8(b), which shows that the error is limited at the end of the gate by high-frequency oscillations in the errors of states $\widetilde{|001\rangle}$, $\widetilde{|100\rangle}$, and $\widetilde{|101\rangle}$. Thus altering the gate duration even slightly causes a rather large difference in the total error of the gate, explaining the varying error of the square pulse in Fig. 7(a). These oscillations are naturally explained by the non-adiabatic change in ω_c at the start of the pulse causing unwanted excitations, which limits the performance of the square pulse in comparison to the adiabatic pulse shapes. In Appendix D, it is shown that the evolution of the state coefficient along $\widetilde{|101\rangle}$ is in general mostly dictated by six different eigenstates, implying that it, like the states $\widetilde{|001\rangle}$ and $\widetilde{|100\rangle}$, couples to non-computational states during the pulse.

Figure 8(c) shows the evolution of the different sources of error for the sine pulse. In contrast to the square pulse, there are no high frequency oscillations in the different errors, but instead, for example, the error related to $\widetilde{|101\rangle}$ first increases smoothly and then starts decreasing half-way through the gate operation. This can be understood as the component of the state vector along $\widetilde{|101\rangle}$ shifting with the change of the eigenstate as ω_c departs from ω_c^{off}, and then returning to the original computational state. If the gate duration is set to be too short, however, the adiabatic approximation breaks down since the change in the Hamiltonian has to be relatively fast for $\int_0^T \tilde{g}_e(t)dt = -\pi/2$ to hold. This explains the error of the sine pulse being

larger than the optimal error of the square pulse at short gate durations in Fig. 7, since the maximum deviation of ω_c from ω_c^{off} is larger for the sine pulse than for the square pulse, causing strong non-adiabatic effects.
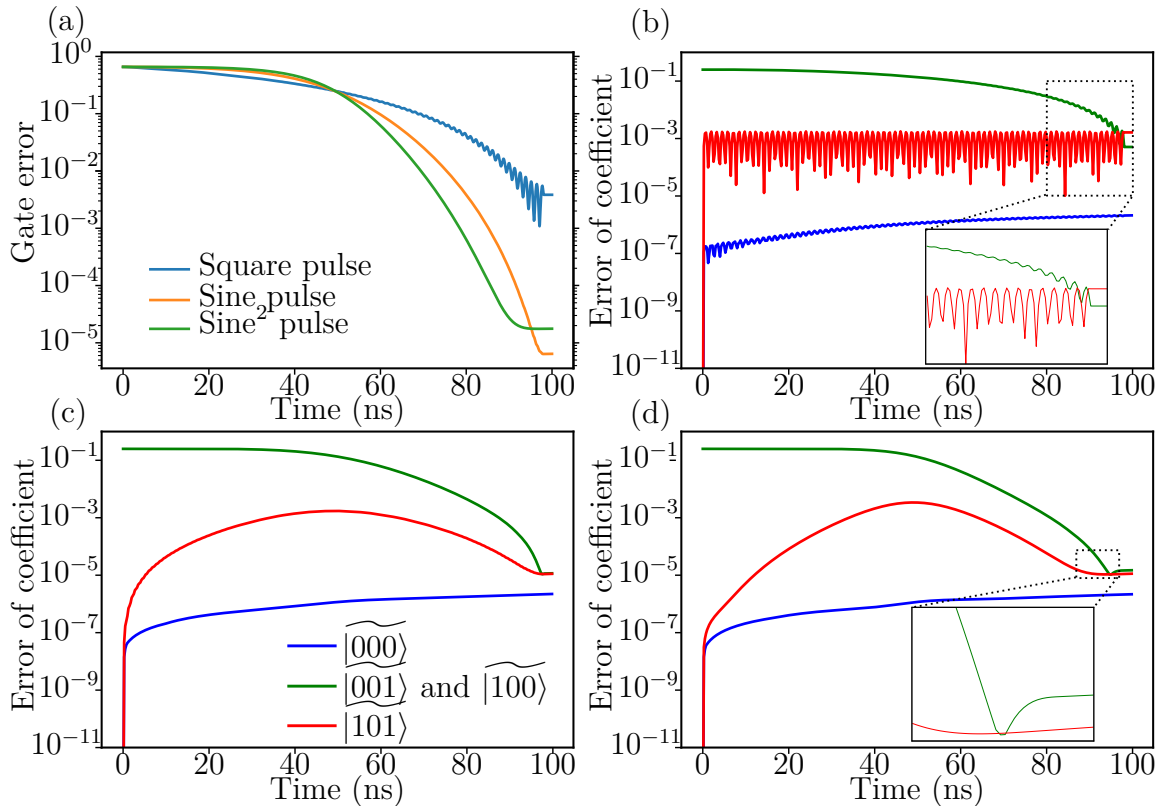

Figure 8: (a) Gate error as a function of time during a gate operation for the different pulse shapes. The gate operation finishes at 98 ns. (b)–(d) The errors related to the coefficients of the computational states during the gate operation for the (b) square, (c) sine, and (d) sine squared pulses. The errors linked to the coefficients of $\widetilde{|001\rangle}$ and $\widetilde{|100\rangle}$ are summed together.

Continuing with the same logic, the sine squared pulse should, at long enough gate durations, produce even lower errors than the sine pulse as there are no discontinuities in the slope of the pulse and the evolution should be accurately adiabatic. This is not, however, the case even at a gate duration of 100 ns. Figure 8(d) reveals that we see that the main source of error in this case are the states $\widetilde{|001\rangle}$ and $\widetilde{|100\rangle}$, with the error reaching a low value before the end of the pulse and then increasing slightly towards the end. This is most likely because the prediction of the pulse shape using $\tilde{g}_e$ does not work correctly for this pulse shape, and the gate operation misses the optimal swapping interaction by a small factor. This may be explained by the fact that the amplitude for the sine squared pulse must be larger than for the sine pulse for any given gate duration, forcing one to adjust ω_c far from ω_c^{off} during the operation.

5   Conclusions

In this thesis, the tunable-coupler system presented in Ref. [13] was simulated and tested in its viability for implementing two-qubit gates. Using a sine pulse on the coupler frequency results in gate errors below 10^{-5} at gate durations of $\sim$100 ns, indicating its ability in implementing high-fidelity gate operations. This also means that the error caused by coupling to non-computational states will not become a limiting factor soon using this system, even though the coherence times of superconducting qubits continue to improve [12]. High fidelity gates are necessary for the realization of a universal error-corrected quantum computer [16], and hence the studied system may become a very relevant option for implementing two-qubit gates in the future.

It is also clear that the shape of the pulse has a major effect when reaching low gate errors and in particular the square pulse does not perform as well as the the sine pulse or the sine squared pulse in reaching very low errors. This is explained by non-adiabatic changes in the system causing coupling to non-computational states. While better than the square pulse at gate durations of over 50 ns, the sine squared pulse does not perform as well as the sine pulse for any of the simulated gate durations. The difference is likely mostly caused by non-optimal pulse parameters when using the sine squared pulse.

There are a number of ways to improve the gate fidelity even further. Optimizing the parameters of the sine squared pulse should result in lower error than what we obtained. Coupling to non-computational states could be reduced by adjusting the system parameters, such as the anharmonicities of the qubits. For the best possible fidelities using a given system, optimized pulse shaping methods such as the gradient ascent pulse engineering algorithm (GRAPE) [20] and the chopped random basis (CRAB) algorithm [21] could be used.

References

[1] Steane, A. Quantum computing. *Reports on Progress in Physics* **61,** 117–173 (1998).

[2] Shor, P. W. Polynomial-Time Algorithms for Prime Factorization and Discrete Logarithms on a Quantum Computer. arXiv: `quant-ph/9508027` (1995).

[3] Grover, L. K. A fast quantum mechanical algorithm for database search. *Proceedings of the twenty-eighth annual ACM symposium on Theory of computing - STOC '96,* 212–219 (1996).

[4] Georgescu, I. M., Ashhab, S. & Nori, F. Quantum simulation. *Reviews of Modern Physics* **86,** 153–185 (2014).

[5] Feynman, R. P. Simulating physics with computers. *International Journal of Theoretical Physics* **21,** 467–488 (1982).

[6] Shnirman, A., Schön, G. & Hermon, Z. Quantum manipulations of small Josephson junctions. *Physical Review Letters* **79,** 2371–2374 (1997).

[7] Bouchiat, V., Vion, D., Joyez, P., Esteve, D. & Devoret, M. H. Quantum Coherence with a Single Cooper Pair. *Physica Scripta* **T76,** 165 (1998).

[8] Nakamura, Y., Pashkin, Y. A. & Tsai, J. S. Coherent control of macroscopic quantum states in a single-Cooper-pair box. *Nature* **398,** 0–2 (1999).

[9] Martinis, J. M., Nam, S., Aumentado, J. & Urbina, C. Rabi Oscillations in a Large Josephson-Junction Qubit. *Physical Review Letters* **89,** 9–12 (2002).

[10] Koch, J. *et al.* Charge-insensitive qubit design derived from the Cooper pair box. *Physical Review A - Atomic, Molecular, and Optical Physics* **76,** 1–19 (2007).

[11] Manucharyan, V. E., Koch, J., Glazman, L. I. & Devoret, M. H. Fluxonium: Single cooper-pair circuit free of charge offsets. *Science* **326,** 113–116 (2009).

[12] Wendin, G. Quantum information processing with superconducting circuits: a review. *Reports on Progress in Physics* **80,** 106001 (2017).

[13] Yan, F. *et al.* A tunable coupling scheme for implementing high-fidelity two-qubit gates. arXiv: `1803.09813` (2018).

[14] Echternach, P. *et al.* Universal Quantum Gates for Single Cooper Pair Box Based Quantum Computing. *Quantum* **1,** 8 (2001).

[15] Shankar, R. *Principles of quantum mechanics* 2nd (Springer, New York, 2014).

[16] DiVincenzo, D. *Quantum Information Processing: Lecture Notes of the 44th IFF Spring School 2013* (Forschungszentrum Jülich, 2013).

[17] Wendin, G. & Shumeiko, V. S. Superconducting Quantum Circuits, Qubits and Computing. arXiv: `cond-mat/0508729` (2005).

[18] White, A. G. *et al.* Measuring two-qubit gates. *Journal of the Optical Society of America B* **24,** 172 (2007).

[19] Johansson, J. R., Nation, P. D. & Nori, F. QuTiP 2: A Python framework for the dynamics of open quantum systems. *Computer Physics Communications* **184,** 1234–1240 (2013).

[20] Khaneja, N., Reiss, T., Kehlet, C., Schulte-Herbrüggen, T. & Glaser, S. J. Optimal control of coupled spin dynamics: Design of NMR pulse sequences by gradient ascent algorithms. *Journal of Magnetic Resonance* **172,** 296–305 (2005).

[21] Doria, P., Calarco, T. & Montangero, S. Optimal control technique for many-body quantum dynamics. *Physical Review Letters* **106,** 1–4 (2011).

A Simplification of the approximated transmon Hamiltonian

The fact that sum of the six terms in Eq. (46) can be expressed as $-\frac{E_C}{4} - E_C \hat{b}^\dagger \hat{b} - \frac{E_C}{2} \hat{b}^\dagger \hat{b}^\dagger \hat{b} \hat{b}$ is calculated in this appendix. By using the commutation relation $[\hat{b}, \hat{b}^\dagger] = 1$, five of the terms are transformed as

$$\hat{b}^\dagger \hat{b} \hat{b}^\dagger \hat{b} = \hat{b}^\dagger (\hat{b}^\dagger \hat{b} + 1) \hat{b} = \hat{b}^\dagger \hat{b}^\dagger \hat{b} \hat{b} + \hat{b}^\dagger \hat{b}, \tag{A1}$$

$$\hat{b}^\dagger \hat{b} \hat{b} \hat{b}^\dagger = \hat{b}^\dagger \hat{b} (\hat{b}^\dagger \hat{b} + 1) = \hat{b}^\dagger \hat{b}^\dagger \hat{b} \hat{b} + \hat{b}^\dagger \hat{b} + \hat{b}^\dagger \hat{b} = \hat{b}^\dagger \hat{b}^\dagger \hat{b} \hat{b} + 2 \hat{b}^\dagger \hat{b}, \tag{A2}$$

$$\hat{b} \hat{b}^\dagger \hat{b}^\dagger \hat{b} = (\hat{b}^\dagger \hat{b} + 1) \hat{b}^\dagger \hat{b} = \hat{b}^\dagger \hat{b}^\dagger \hat{b} \hat{b} + \hat{b}^\dagger \hat{b} + \hat{b}^\dagger \hat{b} = \hat{b}^\dagger \hat{b}^\dagger \hat{b} \hat{b} + 2 \hat{b}^\dagger \hat{b}, \tag{A3}$$

$$\hat{b} \hat{b}^\dagger \hat{b} \hat{b}^\dagger = \hat{b} \hat{b}^\dagger (\hat{b}^\dagger \hat{b} + 1) = \hat{b}^\dagger \hat{b}^\dagger \hat{b} \hat{b} + 2 \hat{b}^\dagger \hat{b} + \hat{b} \hat{b}^\dagger = \hat{b}^\dagger \hat{b}^\dagger \hat{b} \hat{b} + 3 \hat{b}^\dagger \hat{b} + 1, \tag{A4}$$

$$\hat{b} \hat{b} \hat{b}^\dagger \hat{b}^\dagger = \hat{b} (\hat{b}^\dagger \hat{b} + 1) \hat{b}^\dagger = \hat{b}^\dagger \hat{b}^\dagger \hat{b} \hat{b} + 3 \hat{b}^\dagger \hat{b} + 1 + \hat{b} \hat{b}^\dagger = \hat{b}^\dagger \hat{b}^\dagger \hat{b} \hat{b} + 4 \hat{b}^\dagger \hat{b} + 2, \tag{A5}$$

where previously calculated terms have been used repeatedly in the following calculations. Summation of all of the six terms results in

$$\hat{b}^\dagger \hat{b}^\dagger \hat{b} \hat{b} + \hat{b}^\dagger \hat{b} \hat{b}^\dagger \hat{b} + \hat{b}^\dagger \hat{b} \hat{b} \hat{b}^\dagger + \hat{b} \hat{b}^\dagger \hat{b}^\dagger \hat{b} + \hat{b} \hat{b}^\dagger \hat{b} \hat{b}^\dagger + \hat{b} \hat{b} \hat{b}^\dagger \hat{b}^\dagger = 6 \hat{b}^\dagger \hat{b}^\dagger \hat{b} \hat{b} + 12 \hat{b}^\dagger \hat{b} + 3. \tag{A6}$$

Multiplying the sum by $-\frac{E_C}{12}$, we obtain the result used in the main text

$$-\frac{E_C}{12} (6 \hat{b}^\dagger \hat{b}^\dagger \hat{b} \hat{b} + 12 \hat{b}^\dagger \hat{b} + 3) = -\frac{E_C}{4} - E_C \hat{b}^\dagger \hat{b} - \frac{E_C}{2} \hat{b}^\dagger \hat{b}^\dagger \hat{b} \hat{b}. \tag{A7}$$

B Interpretation of the numerically calculated effective interaction strength

This appendix discusses the interpretation of the effective interaction strength $\tilde{g}_e$ and its usage for the square pulse and for the adiabatic pulse shapes. For the square pulse, the temporal evolution of a combination of $\widetilde{|001\rangle}$ and $\widetilde{|100\rangle}$ is calculated by its projecting it on the eigenstates of the system during the pulse. Assuming that during the pulse there are eigenstates close to $\widetilde{|a\rangle} = (\widetilde{|001\rangle} - \widetilde{|100\rangle})/\sqrt{2}$ and $\widetilde{|s\rangle} = (\widetilde{|001\rangle} + \widetilde{|100\rangle})/\sqrt{2}$, the evolution is calculated as

$$\hat{U}(t)(a\widetilde{|001\rangle} + b\widetilde{|100\rangle}) = a(e^{-\frac{i}{\hbar}E_s t}\widetilde{|s\rangle} + e^{-\frac{i}{\hbar}E_a t}\widetilde{|a\rangle}) + b(e^{-\frac{i}{\hbar}E_s t}\widetilde{|s\rangle} - e^{-\frac{i}{\hbar}E_a t}\widetilde{|a\rangle}) \quad \text{(B1)}$$

$$= \left[(e^{-\frac{i}{\hbar}E_s t} + e^{-\frac{i}{\hbar}E_a t})a + (e^{-\frac{i}{\hbar}E_s t} - e^{-\frac{i}{\hbar}E_a t})b \right] \widetilde{|001\rangle}$$
$$+ \widetilde{|100\rangle} \left[(e^{-\frac{i}{\hbar}E_s t} - e^{-\frac{i}{\hbar}E_a t})a + (e^{-\frac{i}{\hbar}E_s t} + e^{-\frac{i}{\hbar}E_a t})b \right] \widetilde{|100\rangle}. \quad \text{(B2)}$$

Defining $E_{avg} = (E_s + E_a)/2$ and $\tilde{g}_e = (E_s - E_a)/(2\hbar)$, it is noticed that $E_s = E_{avg} + \hbar\tilde{g}_e$ and $E_a = E_{avg} - \hbar\tilde{g}_e$. The above expression is thus simplified to

$$\frac{1}{2}e^{-\frac{i}{\hbar}E_{avg}t} \left[(e^{-i\tilde{g}_e t} + e^{i\tilde{g}_e t})a + (e^{-i\tilde{g}_e t} - e^{i\tilde{g}_e t})b \right] \widetilde{|001\rangle}$$
$$+ \frac{1}{2}e^{-\frac{i}{\hbar}E_{avg}t} \left[(e^{-i\tilde{g}_e t} - e^{i\tilde{g}_e t})a + (e^{-i\tilde{g}_e t} + e^{i\tilde{g}_e t})b \right] \widetilde{|001\rangle} \quad \text{(B3)}$$

$$= e^{-\frac{i}{\hbar}E_{avg}t} \left[(a\cos(\tilde{g}_e t) - ib\sin(\tilde{g}_e t)) \widetilde{|001\rangle} + (-ai\sin(\tilde{g}_e t) + b\cos(\tilde{g}_e t)) \widetilde{|100\rangle} \right], \quad \text{(B4)}$$

which produces the iSWAP apart from a global phase when $\tilde{g}_e t = -\pi/2$.

For an adiabatic pulse, one only needs to assume that the eigenstates at the start and end of the pulse approach $\widetilde{|001\rangle} + \widetilde{|100\rangle}$ and $\widetilde{|001\rangle} - \widetilde{|100\rangle}$. The time evolution of a state starting at the antisymmetric or symmetric eigenstate is then given by

$$|\Psi_a(t)\rangle = e^{-\frac{i}{\hbar}\int_0^t E_a(t')dt'} e^{-i\gamma_a} |a[\omega_c(t)]\rangle, \quad \text{(B5)}$$

$$|\Psi_s(t)\rangle = e^{-\frac{i}{\hbar}\int_0^t E_s(t')dt'} e^{-i\gamma_s} |s[\omega_c(t)]\rangle. \quad \text{(B6)}$$

where $\omega_c(0) = \omega_c^{off}$ and $|a(\omega_c)\rangle \to \widetilde{|a\rangle}$ and $|s(\omega_c)\rangle \to \widetilde{|s\rangle}$ as $\omega_c \to \omega_c^{off}$. When the coupler frequency is ω_c^{off} the eigenstates are degenerate. However, as ω_c deviates slightly from the decoupling frequency, the eigenstates become the states $\widetilde{|a\rangle}$ and $\widetilde{|s\rangle}$. Given a starting state $a\widetilde{|001\rangle} + b\widetilde{|100\rangle}$, at the beginning of the pulse it is non-adiabatically projected on $\widetilde{|a\rangle}$ and $\widetilde{|s\rangle}$ and starts adiabatically evolving according to

$$\hat{U}(t)(a\widetilde{|001\rangle} + b\widetilde{|100\rangle}) = a(|\Psi_a(t)\rangle + |\Psi_s(t)\rangle) + b(|\Psi_s(t)\rangle - |\Psi_a(t)\rangle). \quad \text{(B7)}$$

Since the parameter ω_c reverses its path during the pulses, the Berry phases γ_a and γ_s are both zero in this situation. Calculating the time evolution until the end of the

pulse at time T where $\omega_\mathrm{c} = \omega_\mathrm{c}^\mathrm{off}$, we get

$$\hat{U}(t)(a\widetilde{|001\rangle} + b\widetilde{|100\rangle}) = \tag{B8}$$

$$e^{-\frac{i}{\hbar}\int_0^T E_\mathrm{avg}\mathrm{d}t}\left[\cos\left(\int_0^T \tilde{g}_\mathrm{e}(t)\mathrm{d}t\right)\widetilde{|001\rangle} - i\sin\left(\int_0^T \tilde{g}_\mathrm{e}(t)\mathrm{d}t\right)\widetilde{|100\rangle}\right] \tag{B9}$$

$$+ e^{-\frac{i}{\hbar}\int_0^T E_\mathrm{avg}\mathrm{d}t}\left[-i\sin\left(\int_0^T \tilde{g}_\mathrm{e}(t)\mathrm{d}t\right)\widetilde{|001\rangle} + \cos\left(\int_0^T \tilde{g}_\mathrm{e}(t)\mathrm{d}t\right)\widetilde{|100\rangle}\right] \tag{B10}$$

where it has again been defined that $E_\mathrm{avg}(t) = [E_\mathrm{s}(t) + E_\mathrm{a}(t)]/2$ and $\tilde{g}_\mathrm{e}(t) = [E_\mathrm{s}(t) - E_\mathrm{a}(t)]/(2\hbar)$. Thus we observe that the condition $\int_0^T \tilde{g}_\mathrm{e}(t)\mathrm{d}t = -\pi/2$ results in the iSWAP gate in this case as well.

C   Error of the swapping interaction using the square pulse

As discussed in Sec. 4.1, in general the time evolution after applying a square pulse is not exactly the simple swapping interaction between states $\widetilde{|001\rangle}$ and $\widetilde{|100\rangle}$, but instead the coupling to other states must be taken in to account. For instance, the Figs. 4(b)–(d) show that to calculate the temporal evolution of states $\widetilde{|001\rangle}$ and $\widetilde{|100\rangle}$, one must take in to account the three eigenstates of the form

$$|1\rangle = a(\widetilde{|001\rangle} + \widetilde{|100\rangle}) - \sqrt{1 - 2a^2}\widetilde{|010\rangle}, \tag{C1}$$

$$|2\rangle = \frac{1}{\sqrt{2}}(\widetilde{|001\rangle} - \widetilde{|100\rangle}), \tag{C2}$$

$$|3\rangle = b(\widetilde{|001\rangle} + \widetilde{|100\rangle}) + \sqrt{1 - 2b^2}\widetilde{|010\rangle},, \tag{C3}$$

with eigenenergies E_1, E_2, and E_3, respectively, in ascending order. In this section, the evolution of a state starting from $\widetilde{|001\rangle}$ is calculated. We start by noting that the eigenstates $|1\rangle$ and $|3\rangle$ have to be orthonormal, $\langle 1|3\rangle = 0$, which results in the identity

$$\frac{\sqrt{1 - 2a^2}}{\sqrt{1 - 2b^2}}b = \frac{1 - 2a^2}{2a}, \tag{C4}$$

The computational state $\widetilde{|001\rangle}$ is projected on the eigenstates with

$$\widetilde{|001\rangle} \propto |1\rangle + \frac{\sqrt{1 - 2a^2}}{\sqrt{1 - 2b^2}}|3\rangle + \sqrt{2}\left(a + \frac{\sqrt{1 - 2a^2}}{\sqrt{1 - 2b^2}}b\right)|2\rangle. \tag{C5}$$

The time evolution is thus calculated to be

$$\hat{U}(t)\widetilde{|001\rangle} \propto e^{-\frac{i}{\hbar}E_1 t}|1\rangle + e^{-\frac{i}{\hbar}E_3 t}\frac{\sqrt{1 - 2a^2}}{\sqrt{1 - 2b^2}}|3\rangle + e^{-\frac{i}{\hbar}E_2 t}\sqrt{2}\left(a + \frac{\sqrt{1 - 2a^2}}{\sqrt{1 - 2b^2}}b\right)|2\rangle. \tag{C6}$$

Inserting the definitions from Eqs. (C1)–(C3), grouping terms and using the identity (C4), we obtain

$$\hat{U}(t)\widetilde{|001\rangle} \propto \sqrt{1 - 2a^2}\left(e^{-\frac{i}{\hbar}E_3 t} - e^{-\frac{i}{\hbar}E_1 t}\right)\widetilde{|010\rangle}$$
$$+ \left[ae^{-\frac{i}{\hbar}E_1 t} + \frac{1 - 2a^2}{2a}e^{-\frac{i}{\hbar}E_3 t} + \left(a + \frac{1 - 2a^2}{2a}\right)e^{-\frac{i}{\hbar}E_2 t}\right]\widetilde{|001\rangle}$$
$$+ \left[ae^{-\frac{i}{\hbar}E_1 t} + \frac{1 - 2a^2}{2a}e^{-\frac{i}{\hbar}E_3 t} - \left(a + \frac{1 - 2a^2}{2a}\right)e^{-\frac{i}{\hbar}E_2 t}\right]\widetilde{|100\rangle}. \tag{C7}$$

Next is is useful to define the average energies of the different eigenstates $E_{1,2}^{\mathrm{avg}} = \frac{E_1 + E_2}{2}, E_{2,3}^{\mathrm{avg}} = \frac{E_2 + E_3}{2}, E_{1,3}^{\mathrm{avg}} = \frac{E_1 + E_3}{2}$, and the coupling strengths $g_{1,2} = \frac{E_1 - E_2}{2\hbar}, g_{2,3} =$

$\frac{E_2 - E_3}{2\hbar}$, and $g_{1,3} = \frac{E_1 - E_3}{2\hbar}$. Expressing $E_1, E_2,$ and E_3 using these definitions and regrouping, we finally arrive at

$$
\begin{aligned}
\hat{U}(t)\widetilde{|001\rangle} \propto\ & -\sqrt{1 - 2a^2}\, e^{-\frac{i}{\hbar}E_{1,3}^{\mathrm{avg}}t}\, 2i \sin(g_{1,3}t)\widetilde{|010\rangle} \\
& + \left[ae^{-\frac{i}{\hbar}E_{1,2}^{\mathrm{avg}}t}2\cos(g_{1,2}t) + \frac{1 - 2a^2}{2a}e^{-\frac{i}{\hbar}E_{2,3}^{\mathrm{avg}}t}\cos(g_{2,3}t) \right]\widetilde{|001\rangle} \\
& + \left[-ae^{-\frac{i}{\hbar}E_{1,2}^{\mathrm{avg}}t}2i\sin(g_{1,2}t) + \frac{1 - 2a^2}{2a}e^{-\frac{i}{\hbar}E_{2,3}^{\mathrm{avg}}t}i\sin(g_{2,3}t) \right]\widetilde{|100\rangle}. \quad\text{(C8)}
\end{aligned}
$$

Thus, an extra modulation with frequency $g_{2,3}$ is added on top of the swapping interaction. An identical calculation is straightforward for the state $\widetilde{|100\rangle}$ as well. We observe Fig. 4(b)–(d) that if $\omega_c \approx \omega$, the amplitudes of the two oscillations are of similar size, and hence the time evolution can not be considered as a simple swapping operation. On the other hand, if $\omega_c \to \omega_c^{\mathrm{off}}$, $a \to \frac{1}{\sqrt{2}}$ and the expression simplifies to the simple swapping evolution.

D The coupling of state $|\widetilde{101}\rangle$ to non-computational states

Figure D1 visualizes the eigenstates that cause the coupling between $|\widetilde{101}\rangle$ and non-computational states. As the sum of the squared absolute values of the coefficients along states $|\widetilde{101}\rangle, |\widetilde{110}\rangle, |\widetilde{011}\rangle, |\widetilde{020}\rangle, |\widetilde{200}\rangle, |\widetilde{002}\rangle$ equals close to 1 for all ω_c, the eigenstates are almost entirely within the subspace spanned by these states. This implies that the temporal evolution of an initial state $|\widetilde{101}\rangle$ for a non-adiabatic pulse is dominated by the six shown eigenstates.
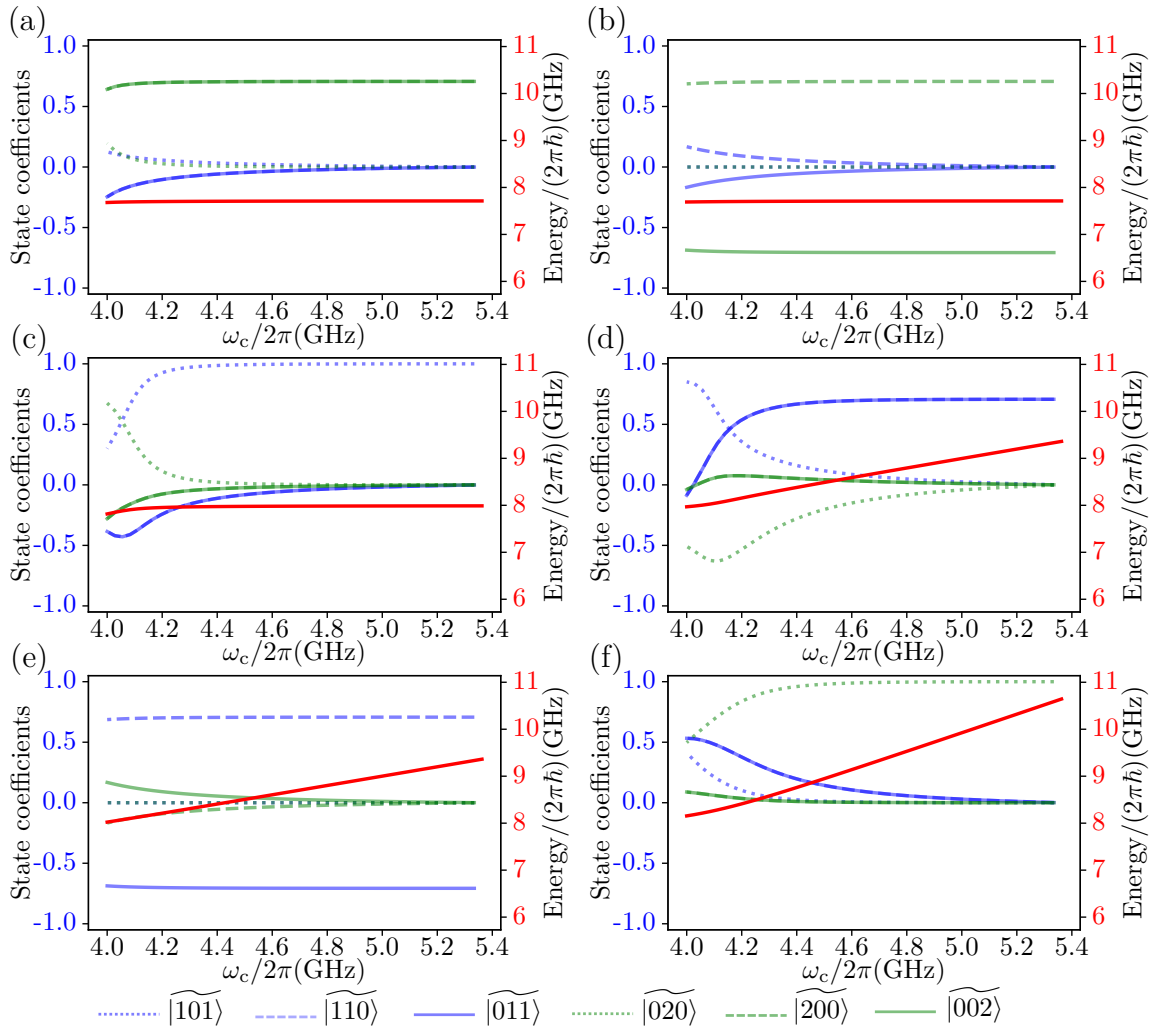

Figure D1: (a)–(f) Coefficients of the eigenstates relevant to the time evolution of state $|\widetilde{101}\rangle$ in the indicated basis as functions of the coupler frequency. Panel (c) shows the eigenstates that are close to $|\widetilde{101}\rangle$ for high ω_c. The sum of the coefficients squared on all of the eigenstates reaches a value of 0.99999986 at its lowest, implying that the eigenstates are almost entirely within the subspace spanned by $|\widetilde{101}\rangle, |\widetilde{110}\rangle, |\widetilde{011}\rangle, |\widetilde{020}\rangle, |\widetilde{200}\rangle$, and $|\widetilde{002}\rangle$, and vice versa.